DEPARTMENT OF DEFENSE UNITED STATES OF AMERICA

Defense Nuclear Agency
Alexandria, VA 22310-3398

DNA-TR-96-20

Improved Fragmentation Algorithms for Debris Environments

Donald R. Curran
James D. Colton
SRI International
333 Ravenswood Avenue
Menlo Park, CA 94025-3434

September 1996

Technical Report

CONTRACT No. DNA 001-93-C-0104

DESTRUCTION NOTICE:

Destroy this report when it is no longer needed.
Do not return to sender.

PLEASE NOTIFY THE DEFENSE SPECIAL WEAPONS AGENCY, ATTN: CSTI, 6801TELEGRAPH ROAD, ALEXANDRIA, VA 22310-3398, IF YOUR ADDRESS IS INCORRECT, IF YOU WISH IT DELETED FROM THE DISTRIBUTION LIST, OR IF THE ADDRESSEE IS NO LONGER EMPLOYED BY YOUR ORGANIZATION.

CUT HERE AND RETURN

DISTRIBUTION LIST UPDATE

This mailer is provided to enable DSWA to maintain current distribution lists for reports. (We would appreciate your providing the requested information.)

☐ Add the individual listed to your distribution list.

☐ Delete the cited organization/individual.

☐ Change of address.

NOTE:
Please return the mailing label from the document so that any additions, changes, corrections or deletions can be made easily. For distribution cancellation or more information call DSWA/IMAS (703) 325-1036.

NAME: ____________________

ORGANIZATION: ____________________

OLD ADDRESS	CURRENT ADDRESS

TELEPHONE NUMBER: (   ) ____________________

DSWA PUBLICATION NUMBER/TITLE	CHANGES/DELETIONS/ADDITIONS, etc.) *(Attach Sheet if more Space is Required)*

DSWA OR OTHER GOVERNMENT CONTRACT NUMBER: ____________________

CERTIFICATION OF NEED-TO-KNOW BY GOVERNMENT SPONSOR (if other than DSWA):

SPONSORING ORGANIZATION: ____________________

CONTRACTING OFFICER OR REPRESENTATIVE: ____________________

SIGNATURE: ____________________

DEFENSE SPECIAL WEAPONS AGENCY
ATTN: IMAS
6801 TELEGRAPH ROAD
ALEXANDRIA, VA 22310-3398

DEFENSE SPECIAL WEAPONS AGENCY
ATTN: IMAS
6801 TELEGRAPH ROAD
ALEXANDRIA, VA 22310-3398

REPORT DOCUMENTATION PAGE

Form Approved
OMB No. 0704-0188

1. AGENCY USE ONLY (Leave blank)

2. REPORT DATE
960901

3. REPORT TYPE AND DATES COVERED
Technical 930520 – 950131

4. TITLE AND SUBTITLE
Improved Fragmentation Algorithms for Debris Environments

5. FUNDING NUMBERS
C - DNA 001-93-C-0104
PE - 63216C, 63214C
PR - SB, AJ
TA - AE, AF
WU - DH336480
DH336490

6. AUTHOR(S)
Donald R. Curran and James D. Colton

7. PERFORMING ORGANIZATION NAME(S) AND ADDRESS(ES)
SRI International
333 Ravenswood Avenue
Menlo Park, CA 94025-3434

8. PERFORMING ORGANIZATION REPORT NUMBER
PYU-4727

9. SPONSORING/MONITORING AGENCY NAME(S) AND ADDRESS(ES)
Defense Special Weapons Agency
6801 Telegraph Road
Alexandria, VA 22310-3398
WELR/Hunter

10. SPONSORING/MONITORING AGENCY REPORT NUMBER
DNA-TR-96-20

11. SUPPLEMENTARY NOTES
This work was sponsored by the Strategic Defense Initiative Office (SDIO), managed and executed by the Defense Special Weapons Agency under RDT&E RMC Code B7668D SB AE 00002 7010A AJ 25904D, B7668D AJ AE 00002 7010A 25904D and B7666D AJ AF 00012 7010A 25904D.

12a. DISTRIBUTION/AVAILABILITY STATEMENT
Approved for public release; distribution is unlimited.

12b. DISTRIBUTION CODE

13. ABSTRACT (Maximum 200 words)

In this report, we describe improved algorithms for fragmentation of targets intercepted by hit-to-kill vehicles or high velocity fragments. The algorithms fall into two classes: (1) direct fragmentation resulting from the intercept, and (2) fragmentation of portions of the target that are directly in contact with high explosive that has itself been initiated by the intercept. The Class 1 case is further subdivided into two subclasses: (a) fragmentation of target material directly adjacent to the impact site, where the fragmentation is caused by interacting high amplitude stress waves, and (b) fragmentation of portions of the target that are undergoing large, dynamic, plastic deformation during structural response, and the stresses are limited in amplitude to the order of the yield strength. In addition, for each of the above cases, we derive algorithms for the fragment shape distributions, and also derive an algorithm for the fragment velocity distribution for the Class 2 case above, explosive fragmentation. Preliminary correlations of the above algorithms with experimental data are shown to be promising.

14. SUBJECT TERMS
Hit-to-Kill
Fragmentation
Structural Response
Debris
Shock Waves

15. NUMBER OF PAGES
48

16. PRICE CODE

17. SECURITY CLASSIFICATION OF REPORT
UNCLASSIFIED

18. SECURITY CLASSIFICATION OF THIS PAGE
UNCLASSIFIED

19. SECURITY CLASSIFICATION OF ABSTRACT
UNCLASSIFIED

20. LIMITATION OF ABSTRACT
SAR

NSN 7540-280-5500

Standard Form 298 (Rev.2-89)
Prescribed by ANSI Sts. 239-18
298-102

CLASSIFIED BY:

N/A since Unclassified.

DECLASSIFY ON:

N/A since Unclassified.

SUMMARY

Fragmentation algorithms are used to predict the debris environment for both spacecraft and ground-based weapons systems experiencing defensive intercepts. Predicting the debris environment is important for target discrimination, system survivability, lethality, and kill assessment. Lethality analyses are currently based on engineering codes that use empirical algorithms. Such fragmentation algorithms serve as input for higher level lethality assessment codes that can perform Monte Carlo shot line analyses, which in turn provide input to still higher level codes that can provide complete assessments of a wide range of outcomes of various interceptor-target engagements. Because the accuracy of the higher level codes depends critically on the uncertainties associated with the algorithms used in the lower level codes, it is important to reduce those uncertainties as much as is practical by basing each algorithm on physical models that are as realistic as possible.

The engineering fragmentation algorithms in current use calculate the fragment mass, size, and velocity distributions, as well as the ballistic coefficients for fragments arising from hypervelocity impacts or explosions, and expected statistical variations in these parameters. The algorithms are largely empirical, but are based on sound dimensional analysis concepts. Specifically, many of the current algorithms are tied to the specific energy coupled to the fragmenting object and the ratio of this coupled specific energy to material-specific fragmentation threshold specific energies. The adjustable parameters in the algorithms are then determined by comparing them with available experimental data.

The work reported here attempts to increase confidence in these algorithms by examining more closely the physical processes of fragmentation and by modifying and extending the algorithms accordingly. We replace algorithmic dependence on coupled specific energy with dependence on average strain rate and basic material properties such as fracture toughness. (Because the average strain rate in the target is often easier to estimate than the coupled specific energy, the new algorithm may be easier to use than the old one.) We add an algorithm to predict the fragment shape distribution. We derive an algorithm for the velocity distribution of explosively driven fragments.

The new algorithms distinguish between between stress wave-driven fragmentation, structural fragmentation, and explosively driven fragmentation. Preliminary correlations with a limited data set are promising.

Recommended future work focuses on correlating the new algorithms with a large portion of the current data base and then extending the predictions to tactical intercepts outside the data base.

CONVERSION TABLE

Conversion factors for U. S. Customary to metric (SI) units of measurement

MULTIPLY → TO GET ←	BY → BY ←		→ TO GET ← DIVIDE
angstrom	1.000 000	X E -10	meters (m)
atmosphere (normal)	1.013 25	X E +2	kilo pascal (kPa)
bar	1.000 000	X E +2	kilo pascal (kPa)
barn	1.000 000	X E -28	meter^2 (m^2)
British thermal unit (thermochemical)	1.054 350	X E +3	joule (J)
calorie (thermochemical)	4.184 000		joule (J)
cal (thermochemical)/cm^2	4.184 000	X E -2	mega joule/m^2 (MJ/m^2)
curie	3.700 000	X E +1	*giga becquerel (GBq)
degree (angle)	1.745 329	X E -2	radian (rad)
degree Fahrenheit	T_K = (T °F+ 459.67)/1.8		degree kelvin (K)
electron volt	1.602 19	X E -19	joule (J)
erg	1.000 000	X E -7	joule (J)
erg/second	1.000 000	X E -7	watt (W)
foot	3.048 000	X E -1	meter (m)
foot-pound-force	1.355 818		joule (J)
gallon (U.S. liquid)	3.785 412	X E -3	meter^3 (m^3)
inch	2.540 000	X E -2	meter (m)
jerk	1.000 000	X E +9	joule (J)
joule/kilogram (J/kg) (radiation dose absorbed)	1.000 000		Gray (Gy)
kilotons	4.183		terajoules
kip (1000 lbf)	4.448 222	X E +3	newton (N)
kip/inch^2 (ksi)	6.894 757	X E +3	kilo pascal (kPa)
ktap	1.000 000	X E +2	newton-second/m^2 (N-s/m^2)
micron	1.000 000	X E -6	meter (m)
mil	2.540 000	X E -5	meter (m)
mile (international)	1.609 344	X E +3	meter (m)
ounce	2.834 952	X E -2	kilogram (kg)
pound-force (lbs avoirdupois)	4.448 222		newton (N)
pound-force inch	1.129 848	X E -1	newton/meter (N · m)
pound-force/inch	1.751 268	X E +2	newton-meter (N/m)
pound-force/foot^2	4.788 026	X E -2	kilo pascal (kPa)
pound-force/inch^2 (psi)	6.894 757		kilo pascal (kPa)
pound-mass (lbm avoirdupois)	4.535 924	X E -1	kilogram (kg)
pound-mass-foot^2 (moment of inertia)	4.214 011	X E -2	kilogram·meter^2 (kg·m^2)
pound-mass-foot^3	1.601 846	X E +1	kilogram/meter^3 (kg/m^3)
rad (radiation dose absorbed)	1.000 000	X E -2	**Gray (Gy)
roentgen	2.579 760	X E -4	coulomb/kilogram (C/kg)
shake	1.000 000	X E -8	second (s)
slug	1.459 390	X E +1	kilogram (kg)
torr (mm Hg, 0° C)	1.333 22	X E -1	kilo pascal (kPa)

*The becquerel (Bq) is the SI unit of radioactivity; 1 Bq = 1 event/s.

**The Gray (Gy) is the SI unit of absorbed radiation.

CONTENTS

FIGURES

FIGURES (Continued)

SECTION 1

INTRODUCTION

Fragmentation algorithms are used to predict the debris environment for both spacecraft and ground-based weapons systems experiencing defensive intercepts. Systems of interest include satellites, boosters, re-entry vehicles, theater missiles, and terrestrial battlefield assets. Predicting the debris environment is important for target discrimination, system survivability, lethality, and kill assessment. Representative engineering codes that use such algorithms include the FAST (Fragmentation Algorithms for Satellite Targets) and FACT (Fragmentation Algorithms for Classified Targets) codes. The algorithms currently used in the FAST and FACT codes are described in a recent report by McKnight, Maher, and Nagl of Kaman Sciences Corporation (1994). (The FACT code addresses theater missile defense engagements.)

Such fragmentation algorithms serve as input for higher level lethality assessment codes (such as KAPP) that can perform Monte Carlo shot line analyses, which in turn provide input to still higher level codes like KELSA, which can provide complete assessments of a wide range of outcomes of various interceptor-target engagements. (A bibliography of such higher level codes has recently been completed by Brosee and Bermudez, 1994.) Because the accuracy of codes like KELSA depends critically on the uncertainties associated with the algorithms used in the lower level codes, those uncertainties must be reduced as much as is practical by basing each algorithm on physical models that are as realistic as possible.

In this report, we attempt to provide physical models for the fragmentation algorithms mentioned above. The engineering fragmentation algorithms in current use calculate the fragment mass, size, and velocity distributions, as well as the ballistic coefficients for fragments arising from hypervelocity impacts or explosions, and expected statistical variations in these parameters. The algorithms are largely empirical, but are based on sound dimensional analysis concepts. Specifically, many of the algorithms are tied to the specific energy (J/g) coupled to the fragmenting object, and the ratio of this coupled specific energy to material-specific, fragmentation, threshold-specific energies. The adjustable parameters in the algorithms are then determined by comparison with available experimental data.

The purpose of the work reported here is to increase confidence in these algorithms (and modify some of them) by examining more closely the physical processes of fragmentation. In addition, we add an algorithm to predict the fragment shape distribution, because of the effect of the shape on the ballistic coefficient.

In Section 2, we discuss the fragmentation processes in detail, and describe the modifications and additions we suggest to the current FAST/FACT algorithms. In Section 3, we summarize the suggested modifications. In Section 4, we correlate the algorithms with a small portion of the current data base. In Section 5, we discuss recommended directions for additional correlations and algorithm development.

SECTION 2

FRAGMENTATION PROCESSES AND ALGORITHM DEVELOPMENT

2.1 BACKGROUND AND APPROACH.

The current fragmentation algorithms in FAST and FACT are based on the specific energy coupled to the fragmenting object, and on material-specific fragmentation energies. Although this approach is a good starting point, we know from extensive prior work (e.g., Curran et al., 1987; Curran and Seaman, 1993) that high rate fracture and fragmentation are processes that result from a competition between loading rates and unloading rates around microcracks that nucleate at inherent microscopic flaws in the material. Sophisticated models have been developed that describe these material-specific processes in detail. A family of such models developed at SRI International is called NAG/FRAG (Nucleation And Growth of microcracks to form FRAGments) (Curran et al., 1987). Our approach is to apply appropriate NAG/FRAG models to the hypervelocity impact and explosive fragmentation cases of interest, and to define the conditions under which these sophisticated models can be simplified to approach either the current algorithms or equally simple algorithms.

2:2 APPLICATION OF NAG/FRAG TO IMPACT-INDUCED FRAGMENTATION.

2.2.1 Fragment Size and Mass Distributions.

2.2.1.1 **Background.** Examinations of fragments from chemical submunitions impacted by hit-to-kill impactor models in sled tests in the Theater Missile Defense (TMD) program suggest that the primary fracture and fragmentation mode is the nucleation, growth, and coalescence of tensile flat cracks (as opposed to shear banding or ductile necking). The fracture surfaces reveal evidence of both ductile void and cleavage crack activity. The appropriate model from the NAG/FRAG family for cleavage cracking is BFRACT, which describes the nucleation, growth, and coalescence of flat cracks to form fragments. Ductile void evolution is modeled by DFRACT (Curran et al., 1987; Curran and Seaman, 1993).

One must next distinguish between extremely high-rate fragmentation caused by reverberating stress waves in the impacted target material, and the much slower fragmentation caused by propagating plastic waves in the target structure. The former case applies in the immediate vicinity of the impact site, whereas the latter applies to parts of the target structure that are many target wall thicknesses removed from the impact site. Most of the "potato chip" fragments collected from the sled tests appear to be caused by the latter mechanism.

Use of the NAG/FRAG models is appropriate in either case. In the first (stress wave) case, BFRACT will produce a fragment size distribution from intersecting cleavage cracks in each failed computational cell, whereas DFRACT will produce no fragments, just a cell that has failed by void coalescence. In the second (plastic wave) case, both BFRACT and DFRACT will describe the macrocracks individually as connected, failed computational cells. In addition, if BFRACT is used, each failed cell will contribute a few fragments on the order of the computational cell size. However, there is in fact no cell size dependence with the NAG/FRAG models because the models contain a microscopically-based scale size that specifies the minimum computational cell size (Curran et al., 1987).

2.2.1.2 <u>Stress Wave-Induced Fragmentation.</u> The actual process (modeled by the NAG/FRAG models) of fragmentation starts with nucleation of microcracks or voids at inherent flaws in the material. How is it then possible that a simplified algorithm (like that in FAST) could be independent of the material-specific flaw size distribution? The answer is that most structural materials contain a very large number of such flaws. Thus, the number of flaws activated may be just the number required to accommodate the available energy.

In this case, the energy balance approach developed by Grady et al. (1985, 1987, 1988) is appropriate. However, unlike the current FAST algorithm, the Grady model for fragment size does not depend on coupled specific energies and material-specific fragmentation energies, but rather on the average strain rate and on the material properties of density, sound speed, and fracture toughness. (On the other hand, as discussed later, one can expect that at sufficiently high impact velocities the number of activated flaws will saturate, and the dependence of fragment size on strain rate will vanish. For the moment, however, consider that the average fragment size depends fundamentally on the strain rate rather than on specific energies.)

The average strain rate can be related to the coupled energy. For example, for a tensile bar pulled plastically at a constant strain rate $\dot{\varepsilon}$, the plastic work per unit volume W done on the bar during the loading time t_o is

$$W = Y\dot{\varepsilon}\, t_o \tag{2.1}$$

where Y is the yield strength. For a given loading time, the Grady formula for calculating the fragment size as a function of strain rate could thus be converted to a dependence on coupled energy through Eq. (2.1). However, the loading time t_o is dependent on the details of the impact and on the impactor and target geometries and sizes, i.e., the relationship between coupled energy and strain rate is target specific. Therefore, if the Grady approach is correct, one can expect that the current FAST algorithm could not be extrapolated to encounters with loading times significantly different than those of the experiments used to calibrate the model.

Fortunately, however, Eq. (2.1) provides guidance on how to modify the FAST algorithm to allow such extrapolation. That is, Grady's formula for the average fragment diameter can be written as

$$s = D(\dot{\varepsilon}) = D(W/Yt_o) = D(\rho EMR/Yt_o) \tag{2.2}$$

where ρ is the density and EMR (energy to mass ratio) is the coupled specific energy used in the FAST code. Thus, the fitted dependence on EMR in FAST for the fragment size could be reinterpreted as a dependence on $\dot{\varepsilon} = \rho EMR/Yt_o$, and then extrapolated to new values of ρ, Y, and t_o.

As mentioned above, the BFRACT model suggests that the Grady approach should fail at very high loading rates near the impact site where all the flaws in the material are activated. In that case, the resulting fragments are on the order of the individual grains in size (the nucleation-dominated region). The Grady approach should also fail at lower loading rates, where only the largest flaws are activated and their subsequent growth to coalescence occurs before smaller flaws become active (the growth-dominated region). Recent work by Curran and Seaman (1993) has extrapolated the Grady approach into these regions. We summarize part of that work.

The approach lies, in complexity, between the full BFRACT treatment and the Grady energy balance approach. In contrast to the energy balance approach, the Curran and Seaman approach contains a dependence on microstructural parameters. We retain the BFRACT dependence on knowledge of the initial flaw size distribution, but simplify the picture by assuming that the flaws are all pre-existing penny-shaped cracks. Then, for a given flaw size distribution and remotely applied stress, we know which flaws are activated (nucleated); they are those with sizes greater than $(K_c/\sigma)^2$, where K_c is the microstructural fracture toughness. That is,

$$R_c \geq (K_c/\sigma)^2 \tag{2.3}$$

where R_c is the critical flaw radius.

Any initial flaw size distribution is allowed, but for purposes of illustration let us assume the commonly observed distribution

$$Ng(R_c) = N_{tc} \exp(-R_c/R_{c1}) \tag{2.4}$$

The c subscripts refer to the flaws (cracks) that have the potential of growing to coalescence to form fragments. N_{tc} is the total number of flaws per unit volume. A minimum fragment diameter can thus be defined; it is

$$s_{min} = N_{tc}^{-1/3}, \; s_{min} > 2 R_{c1} \tag{2.5}$$

That is, if all the flaws grew and coalesced, the average fragment size would be the average distance between the flaw centers (and, of course, the distance between flaw centers is assumed to be greater than the initial flaw sizes).

If we now assume that all active cracks will grow to coalescence, the average fragment diameter will be the spacing between the active crack centers. Thus,

$$s = [Ng(R_c)]^{-1/3} = s_{min} \exp(R_c/3R_{cl}) = s_{min} \exp(K_c^2/3\sigma^2 R_{cl}) \tag{2.6}$$

Following Grady, let σ in Eq. (2.6) be the peak tensile stress, σ_s, and let σ_s be given approximately by

$$\sigma_s = \rho c^2 \dot{\varepsilon}\, t_s \tag{2.7}$$

where t_s is the time at peak stress.

If we assume that $2t_s$ is approximately the time for a crack to propagate the distance s/2 at a velocity of c/3, then

$$t_s = 3s/4c \tag{2.8}$$

Thus, Eqs. (2.6) through (2.8) can be used to solve for σ_s, t_s, and s. Specifically, for s we obtain

$$[\dot{\varepsilon}/A][(s/s_{min})\sqrt{\ln(s/s_{min})}] = 1 \tag{2.9}$$

where $A = 0.8\, K_c/[\rho c s_{min}\sqrt{(R_{cl})}]$. Equation (2.9) is plotted in Figure 2-1, and at strain rates on the order of A gives a dependence of s on strain rate to about a negative 1/2 power, a relation that is similar to the negative 2/3 power dependence produced by the Grady energy balance approach. However, in the present case, the results depend not only on the modulus and K_c, but also on parameters of the initial flaw size distribution, namely s_{min} and R_{c1}. The results are dependent on whether there are large numbers of small flaws (small s_{min} and R_{c1}) or small numbers of large flaws (large s_{min} and R_{cl}).

A suggested modification to the current FAST/FACT algorithms is thus to replace the algorithm for the characteristic fragment size with Eqs. (2.9) and (2.2).

2.2.1.3 **Plastic Deformation-Induced Fragmentation.** However, recall that the above arguments hold only for stress wave-induced fragmentation occurring near the impact site. For the potato chip fragments from the chemical submunitions in the sled tests, it appears more likely that the fractures leading to fragmentation are driven by plastic structural deformations and resultant localized plastic deformation. In that case, Eqs. (2.3), (2.5), and (2.6), with σ given by the yield strength, would be more appropriate for estimating the fragment size distribution. That is, for cracks to propagate and coalesce in a plastically deforming material, the cracks must be larger than the value given by Eq. (2.3), and their

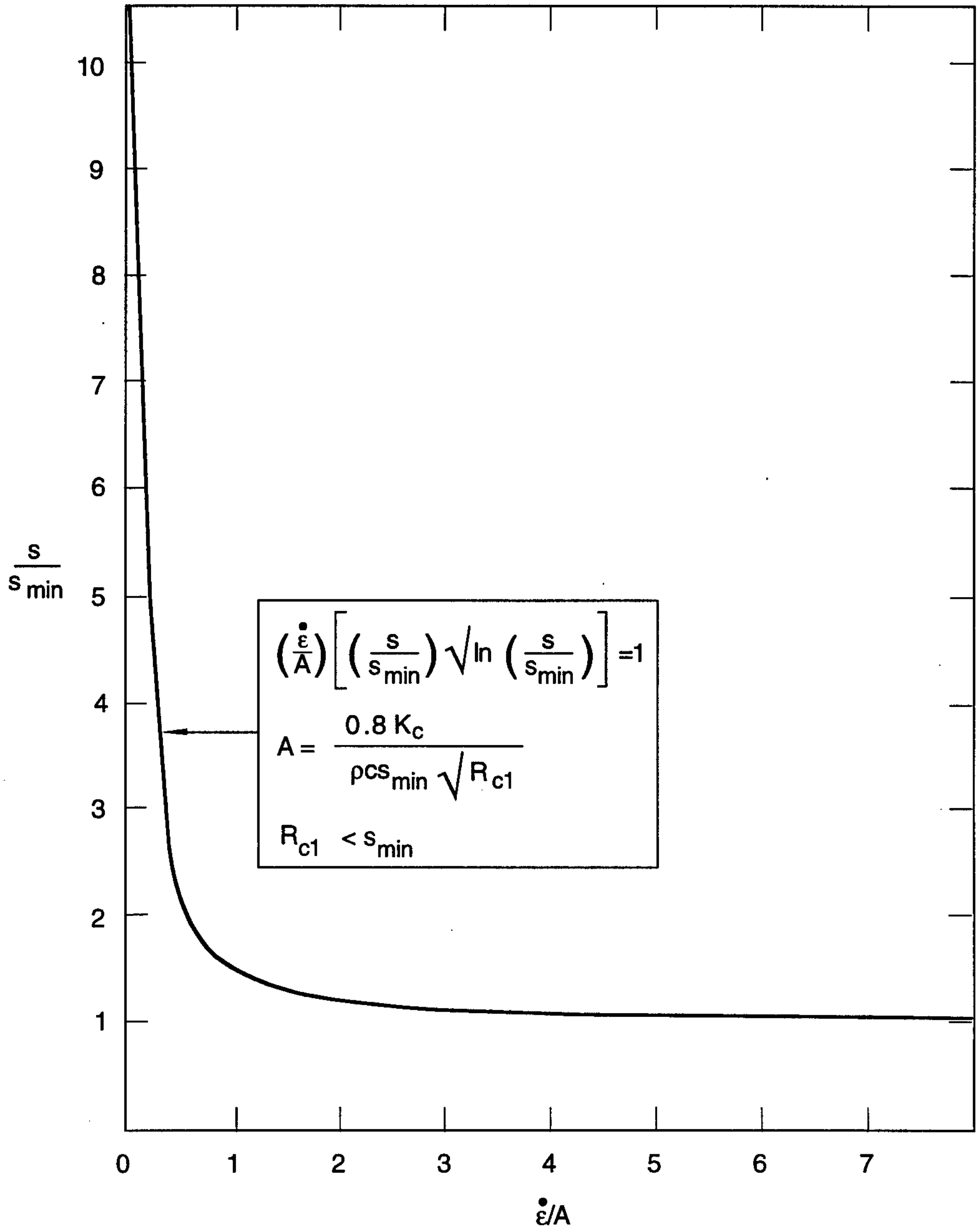

Figure 2-1. Average fragment size as a function of strain rate.

nucleation will occur at plastic strain concentrations in the structure rather than at microscopic flaws. This topic will be discussed in more detail later.

As discussed in Curran and Seaman (1993), the formula for the associated cumulative size distribution is

$$Ng(r) = (1/8\pi s^3)\exp(-2r/s) \qquad (2.10)$$

where Ng(r) is the number of fragments per unit volume with radii greater than r. The current FAST/FACT algorithm uses a power law dependence instead of the above exponential dependence of Ng(r) on r, but both expressions produce similar distributions (many small fragments and fewer large fragments). The mass distributions are obtained from the size distributions by assuming an average fragment shape, as discussed below. (The $1/8\pi s^3$ coefficient in Eq. (2.10) arises from assuming the fragments are spheres.)

2.2.2 Fragment Shape Distributions.

Our current BFRACT model for tensile fracture and fragmentation of solids predicts fragment size distributions but assumes that the fragments are equiaxed. We next derive formulae that relax this assumption, and produce fragment shape distributions in addition to average size distributions (see Eq. (2.17) and Figure 2-5 below). From the shape distributions, we derive associated fragment surface area distributions (see Eq. (2.21) and Figure 2-6 below).

The following derivation applies to both stress wave- and structural response-induced fragmentation. In BFRACT, all the stress wave-induced cracks in a material element have the same orientation. Figure 2-2 illustrates our assumptions. We assume that our material element consists of a stack of columns of square cross section. The central axes of the columns are spaced S apart, where S is the average spacing between crack nucleation sites

$$S = N^{-1/3} \qquad (2.11)$$

and where N is the number of cracks per unit volume in the element. Crack nucleation sites are spaced S apart along each column axis, but the z position of each crack ladder is random. The configuration of Figure 2-2 thus assigns the correct crack density to the material element, but accounts for some of the randomness of the actual nucleation site distribution in a real material by randomly positioning the crack ladders.

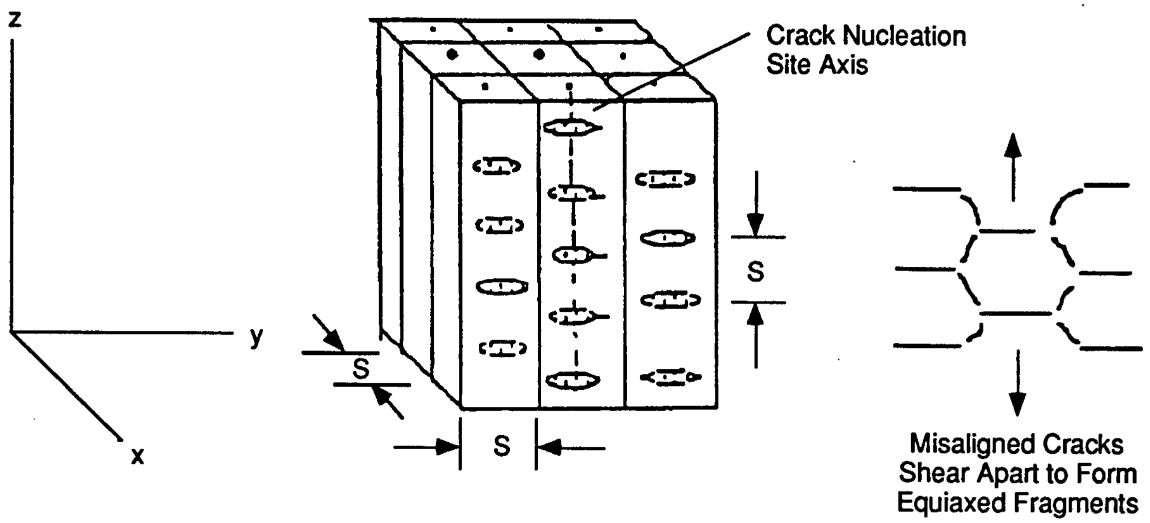

Figure 2-2. Microcrack distribution in a material element.

For plastic deformation-induced fragmentation, we assume that the nucleation of cracks occurs at strain concentrations that also produce patterns of cracks similar to that of Figure 2-2, although they will probably be less aligned. If the cracks in adjacent ladders are not at the same z position, we assume that they will link up by shear cracking. Thus, the cracks in Figure 2-2 would form roughly equiaxed fragments of size S. On the other hand, if the cracks in adjacent ladders are at the same z position, they will coalesce tip-to-tip and form a longer potential fragment.

The probability of adjacent crack tip-to-tip coalescence is the probability that the cracks in adjacent ladders are at the same z position, i.e., the crack tip process zones (PZs)must overlap. Figure 2-3 shows a case where the PZs are on the verge of overlapping. That is

$$p(2) = PZ/S \tag{2.12}$$

where p(2) is the probability that at least two adjacent cracks coalesce. Furthermore, $p(3) = (PZ/S)^2$ and so on, so $p(m) = (PZ/S)^{m-1}$.

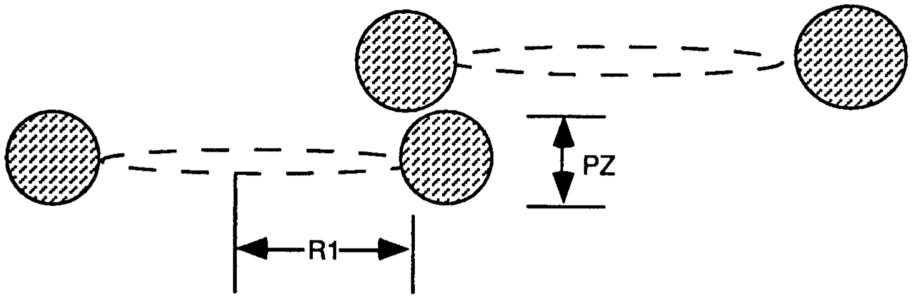

Figure 2-3. Crack coalescence criterion: process zones overlap.

We next introduce the concept of fragment string length, L, which is defined as the shortest length of string required to connect the crack nucleation sites whose cracks form a fragment. This concept is illustrated in Figure 2-4.

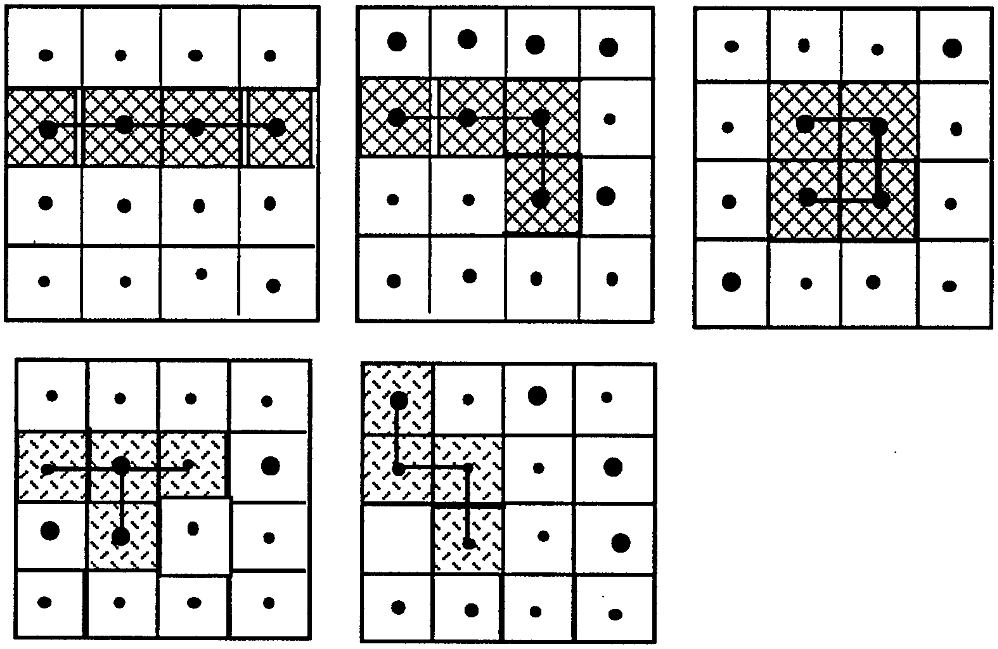

Figure 2-4. Different fragment shapes for a string length of L = 3S (m = 4).

Figure 2-4 shows views down the z axis of Figure 2-2, and illustrates the five different ways in which four adjacent cracks could intersect to form different fragment shapes. Note that the string can have branches. The fragments are all S thick in the z direction. All have equal string lengths of 3S, and all are assumed to be equally probable.

Next, we define an aspect ratio, m:

$$m = 1 + L/S \tag{2.13}$$

where m can also be visualized as the number of cracks that have coalesced in the x-y plane to make the fragment. The probability of a fragment that has an aspect ratio 2 m is thus

$$Ng(m)/N = (PZ/S)^{m-1} \tag{2.14}$$

where Ng(m) is the number of fragments per unit volume with $L/S \geq m - 1$, and N is the total number of fragments per unit volume.

BFRACT calculates a fragment size distribution with a characteristic size of R_{f1}, which is on the order of the average crack size at coalescence. Dimensional analysis shows that, in the absence of strong rate effects,

$$PZ = \beta R_{fl} \tag{2.15}$$

Combine (2.14) and (2.15) to get

$$Ng(m/N = (\beta R_{fl}/S)^{m-1} \tag{2.16}$$

Furthermore, upon coalescence, $R_{fl} \approx S/2$, and thus

$$Ng(m)/N \approx (\beta/2)^{m-1} \tag{2.17}$$

For elastic tensile cracks, $\beta \approx 1$.

2.2.3 Fragment Surface Area Distributions.

The maximum fragment surface area A_{max} (for fragment strings that do not double back) is

$$A_{max} = (2m + 4)S^2 \tag{2.18}$$

Thus, the surface area per unit volume A_{gmax} of the fragments with aspect ratios $\geq$ m is

$$A_{gmax}(S,m) = \int_m^\infty (4 + 2m)S^2(dN/dm)dm \tag{2.19}$$

From Eq. (2.17) we see that

$$dN/dm = -N(\ln a)\, a^{m-1} \tag{2.20}$$

where a = b/2. Solving (2.19) and (2.20) yields

$$A_{gmax}(S,m) = NS^2a^{m-1}[(6 - 2/\ln a) + 2(m-1)] \tag{2.21}$$

where $a < 1$ and $\ln a < 0$.

Figure 2-5 plots Eq. (2.17) for several values of β, and Figure2-6 plots Eq. (2.21) for the same values of β.

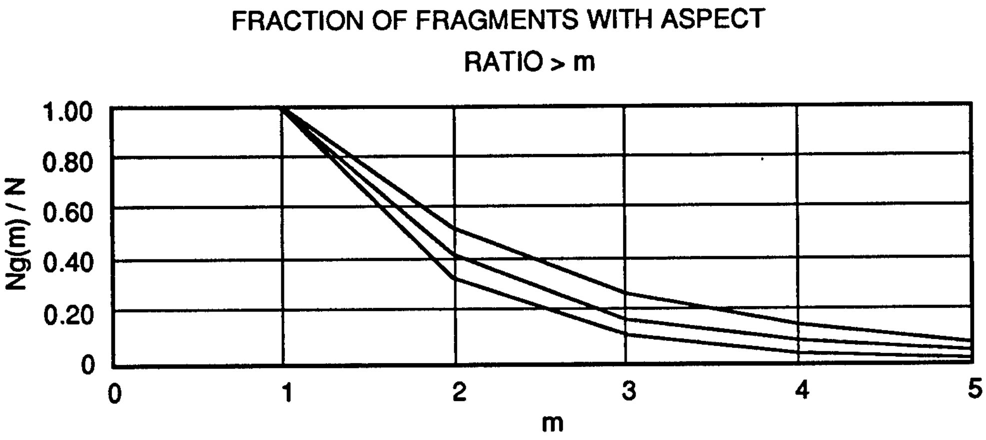

Figure 2-5. Ng(m)/N for a = 0.3, 0.4, and 0.5 (β = 0.6, 0.8, and 1.0).

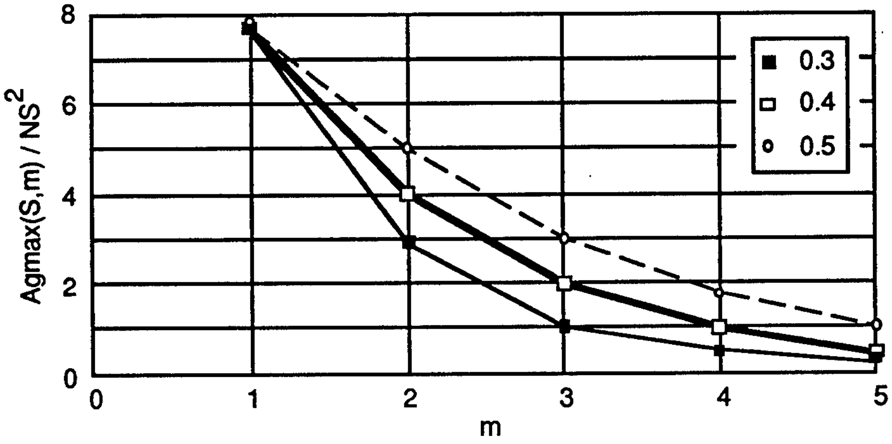

Figure 2-6. Normalized fracture surface area per unit volume for aspect ratios ≥ m, and for values of a = 0.3, 0.4, and 0.5 (β = 0.6, 0.8, and 1.0).

2.2.4 Discussion.

Equation (2.17) should be valid for every fragment shape with the same string length L = (m-l)S. All fragment shapes with the same string length are assumed to be equally probable. Thus, to get the actual fragment shape distribution from (2.17), one must construct pictures like those in Figure 2-4 to see, for each m, how many fragment shapes are possible, and then assign equal numbers of fragments to each possible shape.

Figure 2-4 shows the five possible shapes for m = 4. Thus, we must divide Ng(4) into five equal numbers of fragments of the five possible shapes. It is easy to see that higher values of m will produce many more possible shapes. Figure 2-7 shows 11 possible shapes for m = 5.

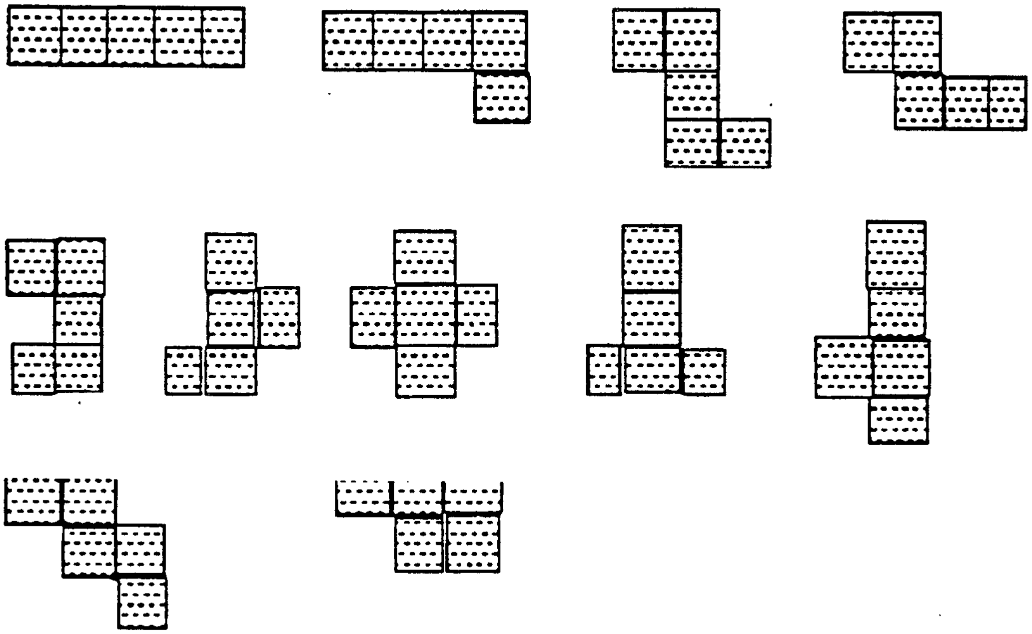

Figure 2-7. Different fragment shapes for string length of L = 4S (m = 5).

Some of the shapes for longer strings (e.g., spirals) would appear to be highly unlikely, but Eq. (2.17) predicts very small numbers of fragments for large m values anyway. Furthermore, such shapes would probably not survive posttest recovery and handling. Thus, Eq. (2.17) should probably only be used with any hope of accuracy for values of $m \leq 5$.

2.2.5 Comparison with Experimental Data.

A reasonable amount of data for novaculite are available, both from plate impact experiments (Shockey et al., 1972) and from explosive and rod impact-induced cratering in novaculite halfspaces (Curran et al., 1977). A view of the inherent flaws in novaculite and some fragments from the experiments are shown in Figures 2-8 through 2-10. BFRACT assumes that the large cracks make large fragments and the smaller cracks make smaller fragments. Under this assumption, Eq. (2.17) can be used for each fragment size range in Figures 2-9 and 2-10. In Figures 2-9 and 2-10, at every size range, the value of β appears to be about 0.6, i.e., about 1/3 of the fragments have $m \geq 2$. The data also appear to be consistent with about 1/10 of the fragments having $m \geq 3$, as predicted by Eq. (2.17) with $\beta = 0.6$ (see Figure 2-5).

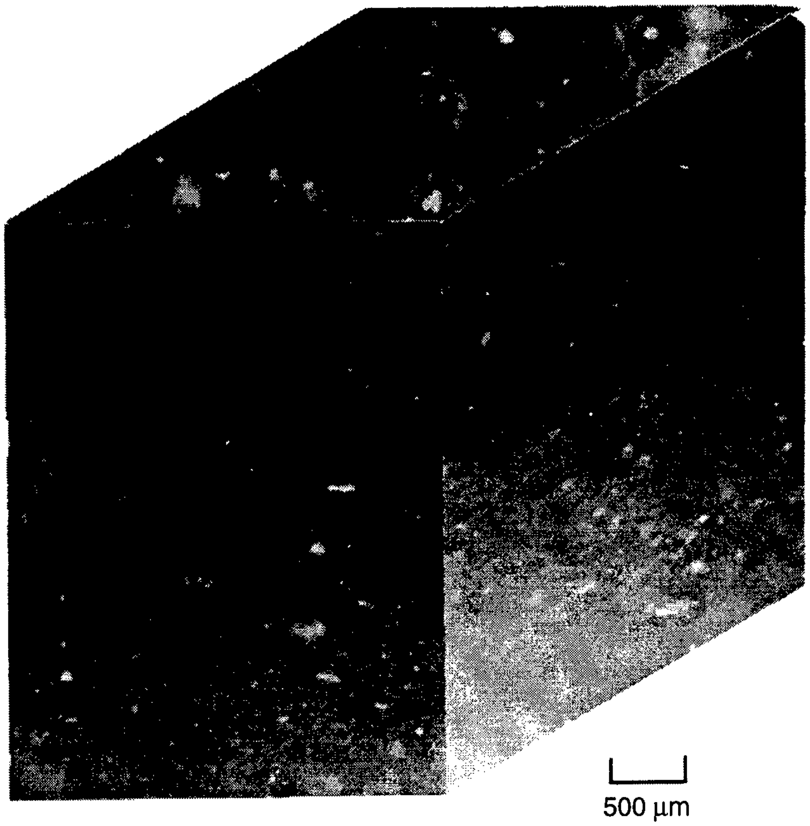

Figure 2-8. Composite micrograph of a block of Arkansas novaculite showing the preferred orientation of preexisting flaws.

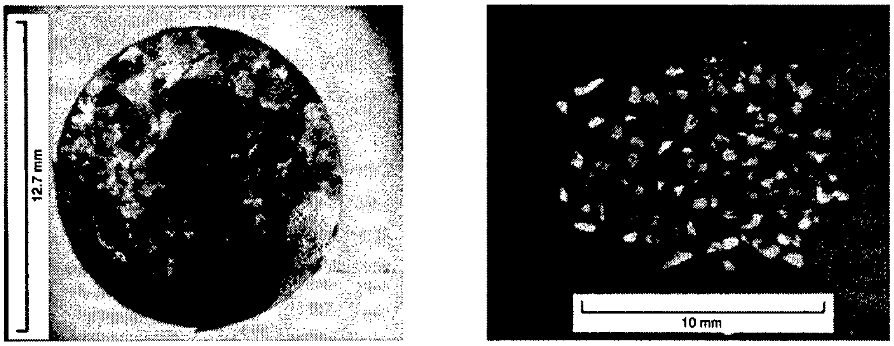

Unfragmented Portion

Radii 149 to 210 µm

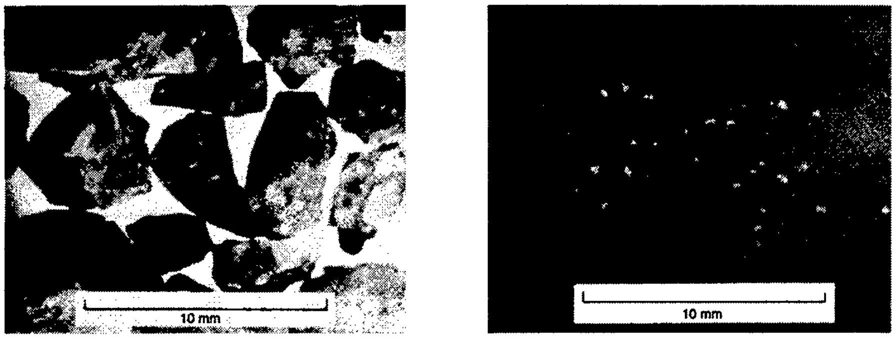

Radii Greater Than 1000 µm

Radii 74 to 149 µm

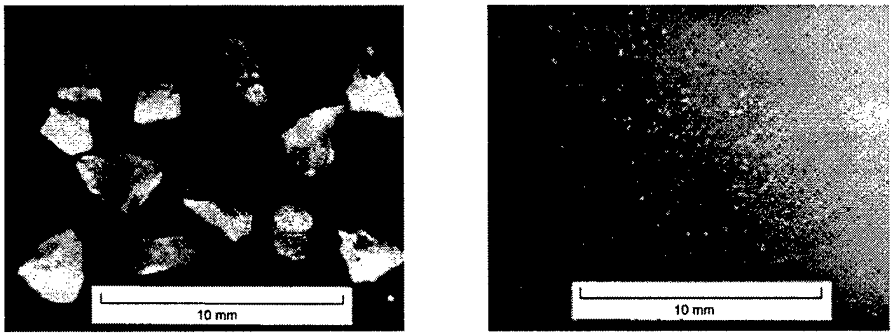

Radii 420 to 1000 µm

Radii 37 to 74 µm

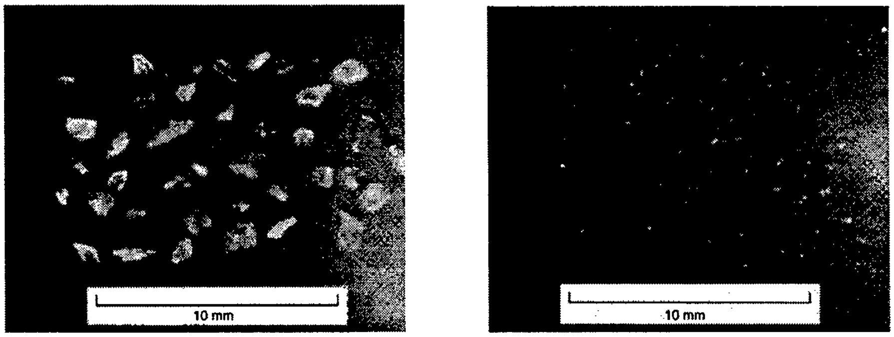

Radii 210 to 420 µm

Radii 18 to 37 µm

Figure 2-9. Photomicrographs of various-sized novaculite fragments from experiment 53 (Shockey, et al.).

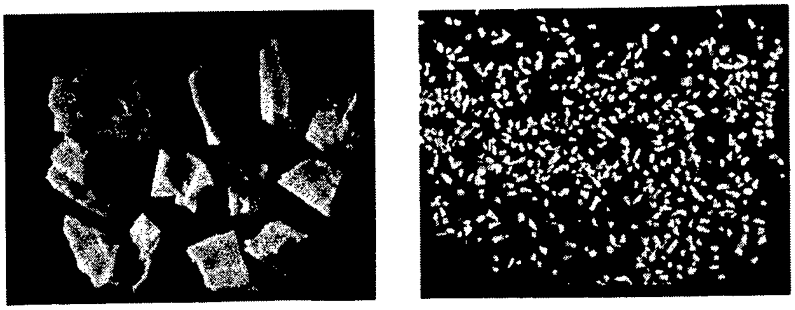

Radii Greater Than 4000 μm

Radii 425 to 600 μm

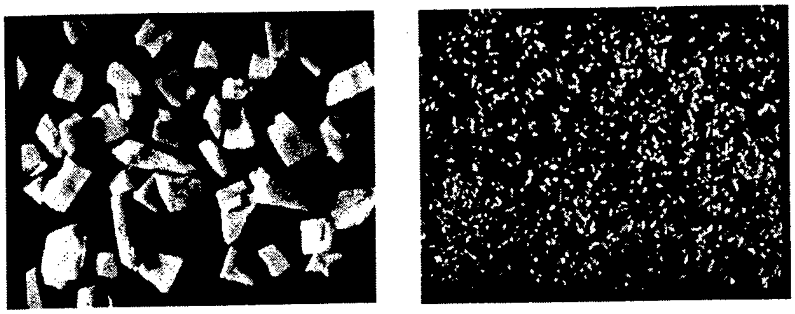

Radii 2000 to 4000 μm

Radii 300 to 425 μm

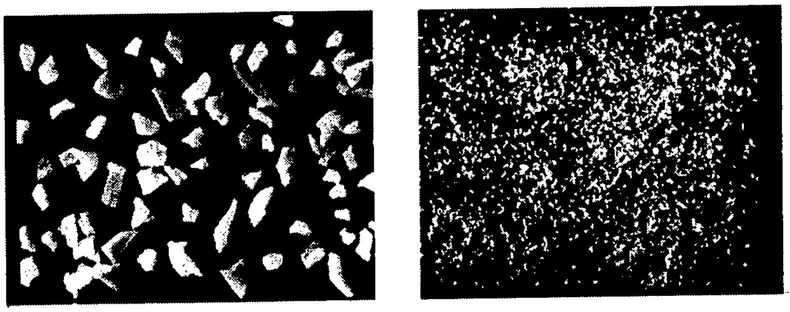

Radii 850 to 2000 μm

Radii 212 to 300 μm

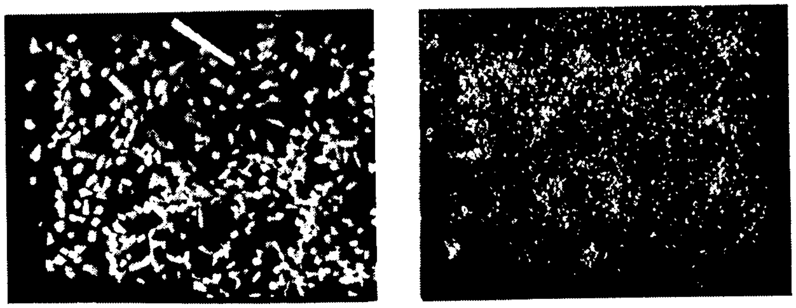

Radii 600 to 850 μm

Radii 150 to 212 μm

1 cm

Figure 2-10. Photomicrographs of various-sized novaculite fragments from experiment G1 (Curran, et al.).

More to the point, we can compare Eqs. (2.9) and (2.17) with fragment size and aspect ratio data from chemical submunition fragments from sled tests. Size distributions and aspect ratios of the fragments from Sled Tests F10 and F11 were measured by Nichols Research Corporation, and the data were kindly provided by Bill Sommers of that organization.

Figure 2-11 shows the size distribution data for the fragments originating from the submunition cylinder walls. Figures 2-12 and 2-13 show the aspect ratio data for the two tests. The theoretical aspect ratio distributions from Eq. (2.17) for several values of β are also shown in Figures 2-12 and 2-13.

Note that Test F11 produced only nine fragments, almost all of them with an aspect ratio of about 2, whereas F10 produced 70 fragments and correspondingly better statistics. We see from Figure 2-11 that the aspect ratio data for F10 agree fairly well with the theoretical formula of Eq. (2.17), with $\beta \approx 0.7$, which is also in rough agreement with the novaculite data ($\beta \approx 0.6$).

As discussed earlier, the fragment size distribution in plastically deforming structures, such as portions of the chemical submunition cannisters that are some distance from the impact site, may be governed by Eqs. (2.3), (2.5), (2.6), and (2.10), with σ set equal to the yield strength Y. That is, we assume that the plastically deforming material will eventually nucleate critically sized cracks at nucleation sites where there are load concentrations. Upon nucleation, the crack size is given by Eq. (2.3), i.e., $R_{c1} \approx (K_c/Y)^2$ in Eq. (2.4).

For the 4340 steel of the chemical submunition cannisters of Tests F10 and F11,

$$K_c \approx 50 \text{ ksi}\sqrt{\text{in.}} = 550 \text{ MPa}\sqrt{\text{cm}}$$

$$Y(\text{dynamic}) \approx 90 \text{ ksi} = 621 \text{ MPa}$$

$$R_{c1} \approx (K_c/Y)^2 = 0.3 \text{ in.} = 0.78 \text{ cm}$$

We next need to estimate the crack nucleation site spacing, s_{min}. Observations of the fragmented submunitions, combined with computational simulations of the deformation of individual canisters, suggest that the cracks nucleate at regions of intense plastic strain, on buckles with spacing on the order of half the cannister circumference. For the Chemical Submunitions 2 of F10 and F11, the outside diameter is 2.5 inches, so

$$s_{min} \approx 10 \text{ cm}$$

Then, Eq. (2.6) (with $\sigma = Y$) yields

$$s \approx 14 \text{ cm}$$

We now rewrite Eq. (2.6) as

$$N_g/N = \exp\{-(M/M_s)^{1/2}\} \qquad (2.6')$$

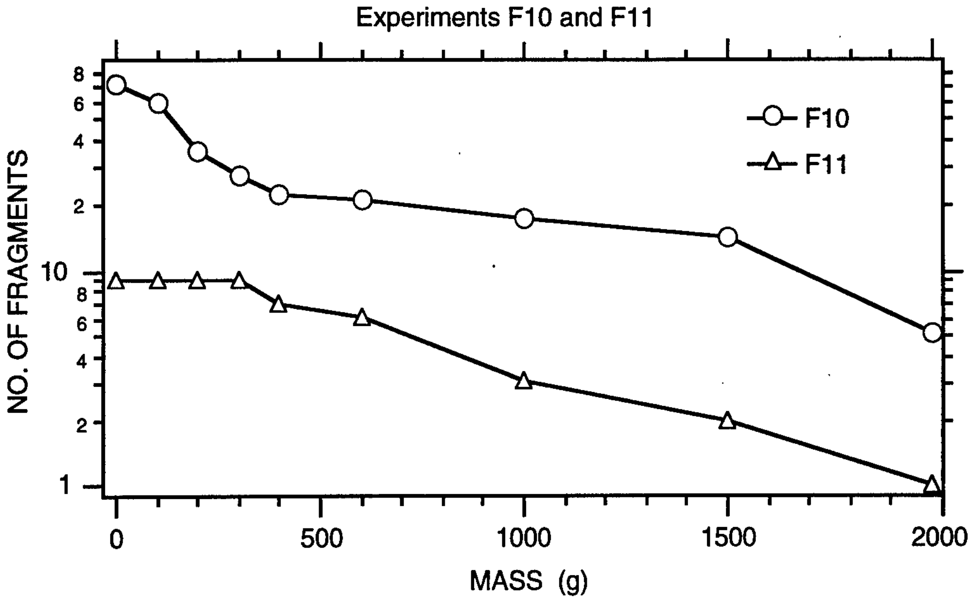

Figure 2-11. Cumulative mass distribution (nnumber of fragments with masses greater than value of abscissa) for fragments from Sled Test F10 and F11.

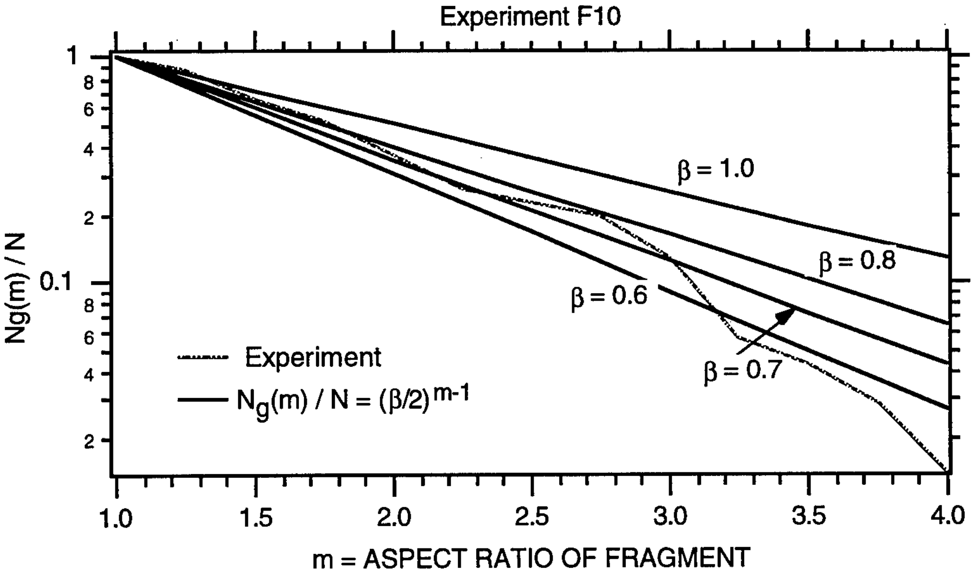

Figure 2-12. Cumulative aspect ratio distribution for Sled Test F10 (fractional number of fragments with aspect ratios greater than m).

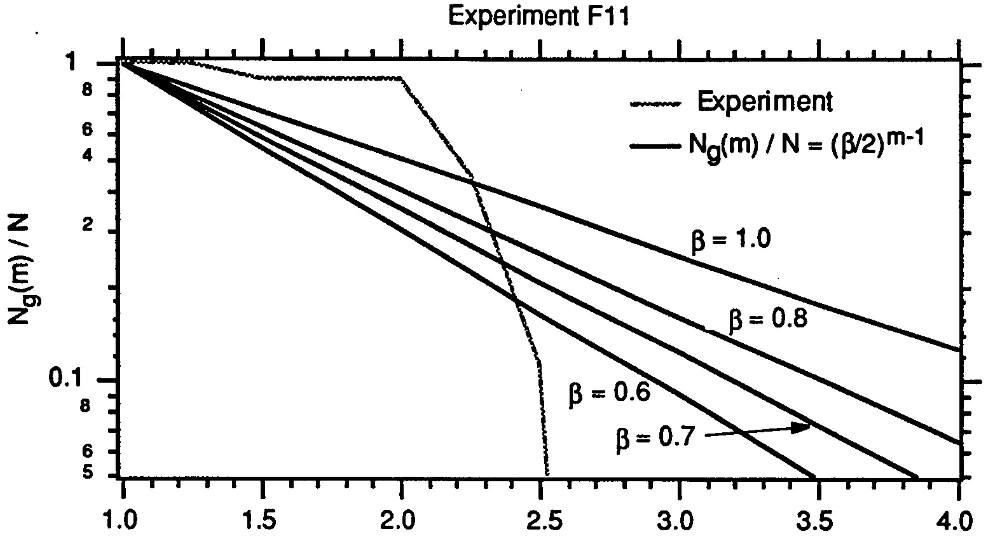

Figure 2-13. Cumulative aspect ratio distribution for Sled Test F11 (fractional number of fragments with aspect ratios greater than m).

where M is the fragment mass, and M_s is the mass associated with the average fragment size, s. The 1/2 exponent arises because the fragments are formed by intersecting through-the-thickness cracks. We define M_s by

$$M_s = \rho s^2 H = 876 \text{ g} \tag{2.6''}$$

where ρ is the steel density (7.84 g/cc), and H is the wall thickness, which is 0.57 cm for the F10 and F11 test articles.

Equation (2.6") is plotted in Figure 2-14, which also shows the normalized data from Figure 2-11. We see that the calculated curve passes between the F10 and F11 data. Of course, the curve's amplitude depends mainly on the value of $M_s(s_{min})$, which in turn depends strongly on the specific structural deformations caused by the impact conditions. (In Sled Test F11, the impactor interacted with the cannister nose piece in such a way to reduce the effect on the cannister, as seen by the reduced number of fragments compared to F10, for which the impactor essentially missed the nose piece.) Computer simulations are needed to obtain a simple algorithm for s_{min}.

2.2.6 Scaling.

A consequence of the above simple theories is that, whereas the fragment size distributions from the impact region should not strictly obey replica scaling laws, the larger fragments from the plastically deforming cannisters should roughly obey replica scaling laws as long as the sample dimensions are larger than the critical crack size R_{c1}. That is, if the cracks in the cannister walls nucleate at regions of localized plastic strain, these regions should obey replica scaling, and the resulting fragmentation will obey replica scaling as long as the nucleated cracks are larger than R_{c1} ($\approx$1 cm for the submunition steel). The fragments formed by detached components such as the nose piece will also obviously obey replica scaling.

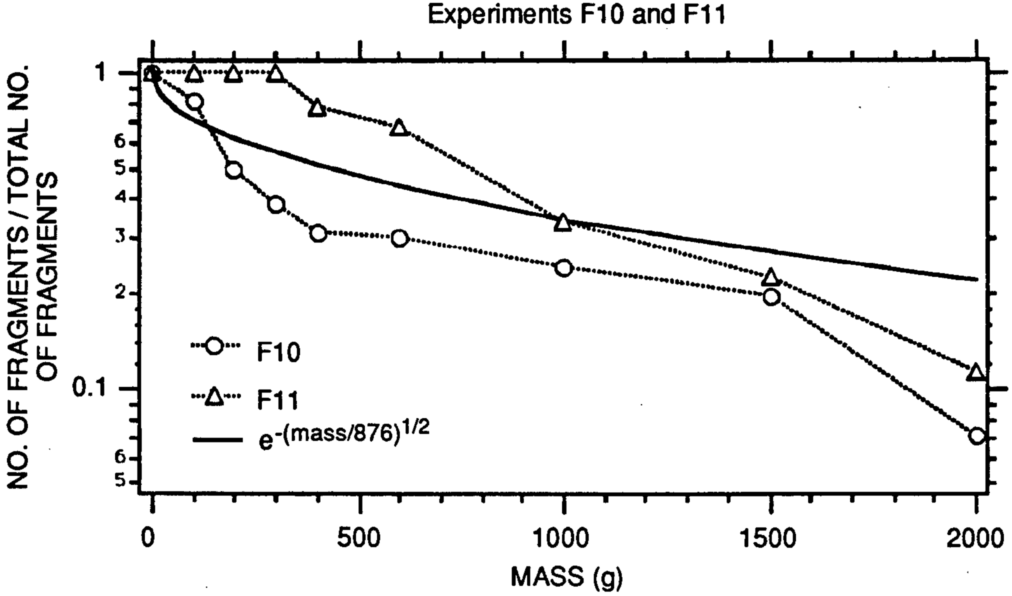

Figure 2-14. Theoretical fragment mass distribution compared with experimental data.

Even the fragments from the impact site may roughly obey replica scaling, if the strain rate puts the material in the elbow of the curve of Figure 2-1, where the average fragment size is roughly inversely proportional to the strain rate. This occurs where the strain rate is somewhat less than A in Eq. (2.9). For the 4340 steel properties given above, and assuming that both s_{min} and R_{c1} are of the order of the microstructural scale ($\approx$ 100 µm), A $\approx$ 10^6/s. Such high strain rates are in fact expected near the impact site. In any event, smaller target components will tend to give smaller fragments from the impact site, so approximate replica scaling is expected.

2.2.7 Conclusions for Fragment Shape and Area Distributions.

Equation (2.17) gives a very simple method of estimating BFRACT fragment shape distributions, and can be used as a simple post-process equation after BFRACT has calculated the equiaxed fragment size distribution. Equation (2.16) is potentially more accurate, and S should ideally be obtained from

Eq. (2.11), where N is the crack concentration at the onset of coalescence. However, since BFRACT does not clearly define the onset of coalescence, but simply tracks the evolution of the damage function τ, it is acceptable, considering the crudeness of the model, to take the value of N when the damage function τ reaches unity. Furthermore, if the approximation leading from Eq. (2.16) to Eq. (2.17) is acceptable, then the result is independent of N anyway.

Thus, the philosophy of the method is to first assume that the fragments are equiaxed, and then tweak that result with Eq. (2.16) or Eq. (2.17). Since these equations predict that most of the fragments will in fact be equiaxed, the method may be acceptable as an approximation. In fact, preliminary correlations with novaculite and sled test fragmentation data show promising agreement between the predictions of Eq. (2.17) and the observations. For applications where the fragment surface area is important (e.g., crack burn models for propellants), Eq. (2.21) may be useful. Algorithms for the fragment size distributions, such as given by Eqs. (2.9) and (2.6'), seem promising as well. All of the above algorithms need testing against more data.

2.3 APPLICATION OF NAG/FRAG TO EXPLOSIVE-INDUCED FRAGMENTATION.

2.3.1 Background.

Fragmentation of target components in direct contact with explosive that has been initiated by an encounter is another process for which past experience and theory are available. Fragmenting, explosively expanded, metal cylinders typically have fragment size distributions consisting of a Poisson size distribution and shape distributions that contain an as yet unquantified mix of equiaxed fragments and fragment strips. The strips are longer in the axial direction than either the wall thickness or the circumferential thickness. At very high loading rates, the fragment circumferential thickness tends to be on the order of the wall thickness. Whereas the circumferential thickness distribution can often be successfully predicted with variations of the Mott (1947) theory or the SRI SHEAR model (Shockey et al., 1985; Curran et al., 1987), the shape variations have heretofore been based more on purely statistical percolation theory than on physical mechanisms (Aharony and Levi, 1986).

It is also common to observe a spreading fragment cloud in time, indicating a distribution of fragment velocities. Such clouds are predicted in computer simulations, but the dominant mechanism is unclear.

We next develop simple physical models to predict the size, shape, and velocity distributions. These models apply only to cases in which the fragmenting material is in direct contact with the explosive.

2.3.2 Simplified Explosive-Induced Fragmentation Models.

The fragmentation of explosive-filled metal containers often occurs by adiabatic shear banding. As described by the NAG/FRAG SHEAR model, the bands nucleate at microscopic heterogeneities with the geometry of penny-shaped or half-penny-shaped cracks, and grow (extend) to coalescence (Curran et al., 1987). As the bands grow in number and size, the average shear stresses decrease due to the reduction of area of intact material (assuming that the bands are thermally softened). That is, the shear stresses in the intact material remain on the yield surface, but the shear stress across a band surface is nearly zero. Therefore, the average (continuum) shear stress will be approximately equal to $Y(1-\Omega)$, where Ω is the fractional area occupied by the bands.

The size of shear bands upon nucleation under dynamic conditions probably depends on strain rate and heat conduction, although many cases may be dominated by geometric softening (Deve et al., 1988; Harren and Asaro, 1989; Meyers et al., 1992). That is, if the flaw is considered to be penny-shaped with a radius, R, adiabatic heating at the band boundary can only occur if the strain concentration at the boundary remains hotter than its surroundings during the nucleation time. This is expressed by the inequality:

$$R \leq \sqrt{\frac{2.5\, k\, \gamma_{cr}}{\dot{\gamma}}} \tag{2.22}$$

where k is the thermal diffusivity, γ_{cr} is the critical strain for localization, and $\dot{\gamma}$ is the strain rate. Thus, the rhs of Eq. (2.22) is the minimum size flaw that can be activated. It is also the minimum possible fragment size, corresponding to instantaneous coalescence of the smallest activated flaws.

For the fragmenting ring experiment of Figure 2-15, where the average strain rate was about $2 \times 10^4\ s^{-1}$ and where the critical localization strain is taken to be about 0.2, the above formula gives a minimum activation band length (2R) less than 50 µm, in agreement with observations.

We may also estimate the average band spacing on nucleation. Grady and Kipp (1987) have estimated the average shear band spacing based on an analysis of the competition between thermal diffusion from the heated band and the unloading wave speed. Assuming a minimum work principle, they derived an average band spacing, 2s, given by the formula:

$$2s = 2[(9\, c^2\, \rho\, k)/(\tau_y\, \alpha^2 \dot{\gamma}^3)]^{1/4} \tag{2.23}$$

where c is the specific heat, ρ is the density, k is the thermal diffusivity, τ_y is the unsoftened shear yielding stress, and α is a linear thermal softening coefficient defined by:

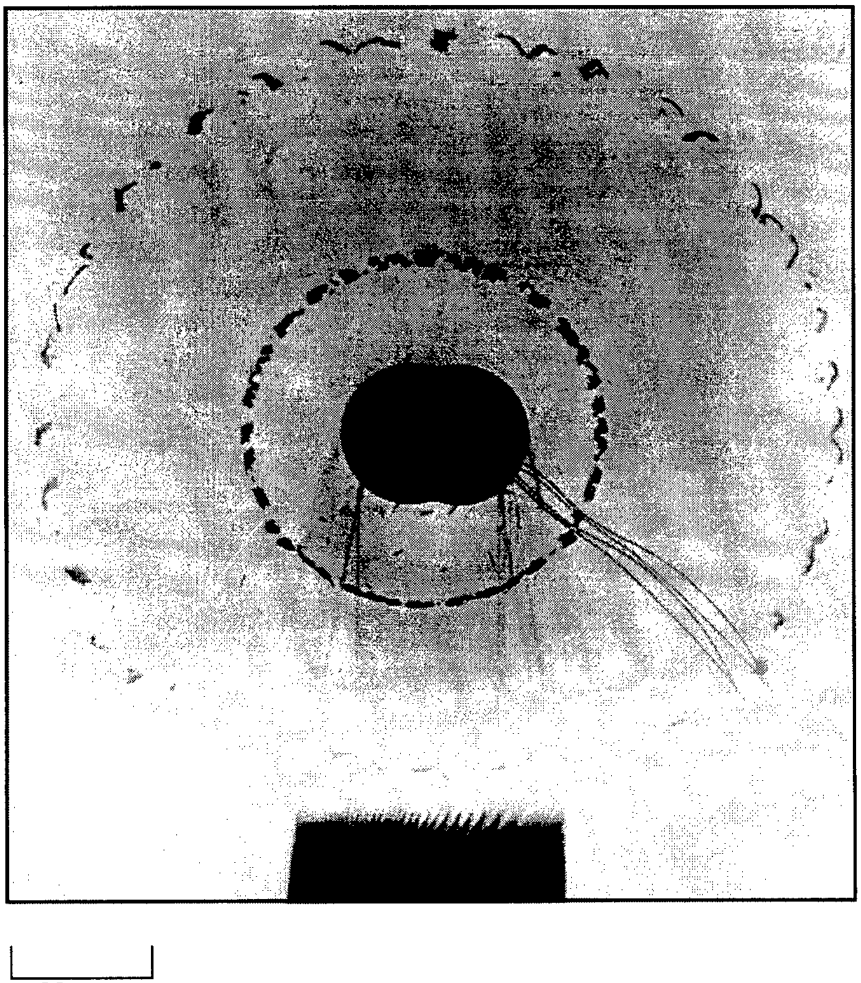

Figure 2-15 Flash x-ray pictures of expanding fragment clouds.

$$\tau = \tau_y[1 + \alpha(T_o - T)] \tag{2.24}$$

where T is the temperature.

Grady and Kipp (1987) interpret 2s from Eq. (2.23) to be the average fragment size. However, this can only be true in the special cases where the nucleated bands intersect specimen free boundaries before they coalesce (as in thin-walled, expanding rings or cylinders, when 2s is the average circumferential fragment dimension), or where all of the nucleated bands coalesce with neighboring bands. In fact, fragments are often observed to contain uncoalesced bands. Thus, Eq. (2.23) should tend to give more numerous and smaller fragments than observed.

For our applications, the complete fragment size distribution not just the average fragment size, is desired. Grady and Kipp (1985) point out that a random Poisson fragmentation process leads to an exponential distribution in fragment size. In fact, the experimental data are often well described by the Poisson distribution:

$$N_g(R) = N_t \exp(-R/R_1) \tag{2.25}$$

where $N_g(R)$ is the number of fragments per unit volume with radii greater than R, N_t is the total fragment concentration, and R_1 is the characteristic size of the distribution. Note that Eq. (2.25) is identical to Eq. (2.4) for cracks.

An interesting feature of this distribution is that the average fragment size R_1, and the average fragment volume (assuming spherical fragments) is $8\pi R_1^3$. As for the argument leading to Eq. (2.10), we assume that a rough estimate of the total fragment concentration is given by:

$$N_t \cong 1/8\pi R_1^3 \tag{2.26}$$

Curran et al. (1993) compare the distribution from Eqs. (2.23) through (2.26) with some limited experimental data and show that the agreement is excellent. Thus, if the average fragment size can be estimated accurately, it appears possible that we can make a remarkably good estimate of the whole distribution for expanding rings and cylinders. More comparisons of this type are needed to explore this possibility.

The simplest model for explosive fragmentation of rings and cylinders has been based for many years on the theory of Mott (1947), who predicted a size distribution around an average fragment size (fragment width in the circumferential direction) given by the formula

$$s = (1.69/\partial\varepsilon/\partial t)(2Y/\rho\gamma)^{1/2} \tag{2.27}$$

where s is the fragment size, ε is the circumferential plastic strain, Y is the yield stress, ρ is the density, and γ is a parameter characterizing the flaw-caused variation of strain-to-failure (between 25 and 100 for many cases).

Mott's theory considers a plastically expanding ring, and assumes that each crack occurs instantaneously and randomly around the ring over a range of strains-to-failure. As the ring strain traverses the range of strains-to-failure, the first crack to appear sends slowly diffusing unloading waves around the ring that protect the material that they traverse from further cracking. The next crack to appear does the same thing, and so on until the ring is completely fragmented. Mott performed a series of such calculations with strains-to-failure randomly assigned from his γ distribution around the circumference for each calculation. From a statistical number of such calculations (in the days before computers!), he derived a size distribution of the Poisson type with the characteristic size given by Eq. (2.27) above.

Mott's theory often gives good agreement with experimental data, but in some circumstances must be modified when the initial assumptions behind the theory are not fulfilled. And in fact, Mott's use of static strain-to-failure data to determine his γ value is basically inaccurate, because the static failure mechanism (coalescence of microcracks or voids) is different from the usual dynamic failure mechanism (coalescence of adiabatic shear bands).

For example, experiments performed by Erlich et al. (1980) show that Eq. (2.27) can easily be misinterpreted. In contained fragmenting cylinder (CFC) experiments, steel cylinders of different yield strengths but identical dimensions were explosively expanded with identical explosive charges, and then the expansions were arrested at identical levels of expansion. According to Eq. (2.27), the steels with higher hardnesses (yield strengths) might be expected to produce larger fragments. In fact, as seen in Figure 2-16, the opposite is true, because the higher hardness steels have less work hardening and thermal softening causes localization into shear bands at lower strain levels. Thus, the failure mechanism and associated strains-to-failure are quite different from those deduced by Mott from static tests. Mott's theory lumps all such effects in the γ parameter. Thus, to get agreement of Eq. (2.27) with the data, the γ parameter would have to be made a strongly increasing function of Y.

Another limitation of Eq. (2.27) arises when the cylinders have walls that are too thick to consider the failure time to be instantaneous. This error can cause Eq. (2.27) to predict values of s that are less than the wall thickness, which is usually not observed because the unloaded region around a shear band roughly equals the wall thickness by the time the band traverses the wall.

These problems with Eq. (2.27) are avoided by using the more sophisticated models of Eqs. (2.23) through (2.26). (Mott's Eq. (2.27) has about the same dependence on strain rate as Eq. (2.23); the difference is that Eqs. (2.23) through (2.26) depend on more relevant material properties.)

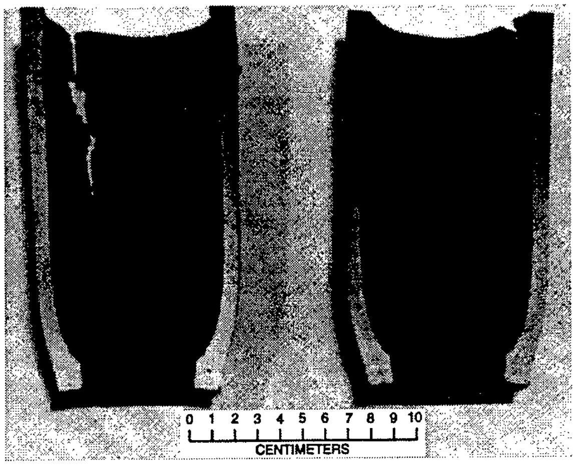

(a) Shot 20, R_C21

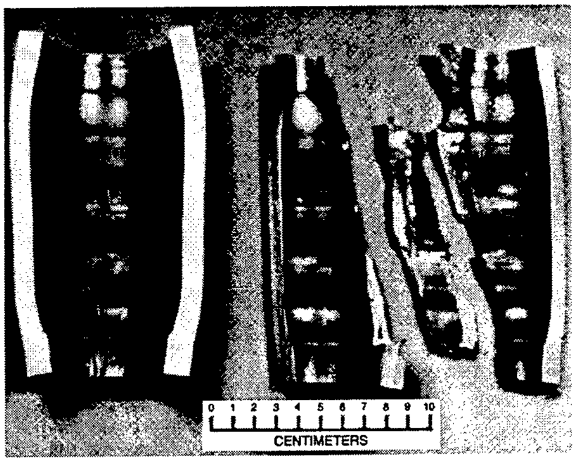

(b) Shot 3, R_C40

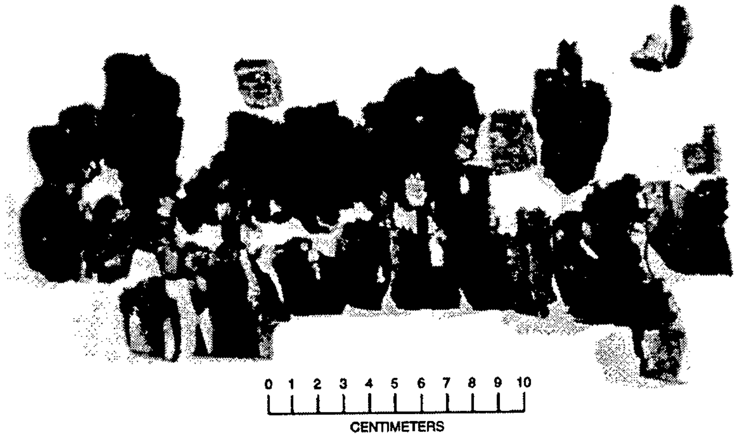

(c) Shot 10, R_C52

Figure 2-16. 4340 steel tubes recovered from three, contained, fragmenting cylinder experiments having identical loading parameters but using specimen materials of different hardness.

In any case, all the above models predict only a size distribution for values of the circumferential width of the fragment. In fact, the fragments also exhibit a distribution of lengths in the cylinder axis direction; strips are produced of various lengths.

We next derive a formula for the strip length distribution.

2.3.3 Fragment Shape Model for Explosive-Induced Fragmentation.

As illustrated in Figures 2-17 and 2-18 from Erlich et al. (1980), the actual fragmentation mechanism in exploding steel cylinders is the nucleation of adiabatic shear bands at points on the inner surface of the cylinder, and extension of these bands outward to form half-penny shaped slip regions with the geometry of macroscopic dislocations of mixed edge and screw types.

Figure 2-19 shows the three main orientations of these bands. The Mode 1 orientation is by far the most common in exploding cylinders, and will be the only mode considered in what follows. As perhaps can be seen in Figures 2-16 through 2-18, the Mode 1 bands occur with equal frequency in the two equivalent directions of maximum resolved shear strain (+ or - 45 degrees from the radial direction).

Figure 2-20 shows the basis of our model, which is a variation of the model described earlier for tensile cracking. We consider the cylinder to be a stack of Mott rings of width equal to the wall thickness H. Each ring has a series of cracks spaced S apart around the ring circumference. If the cracks in adjacent rings are offset, the cracks will eventually tear apart by shear localization between crack tips to form equiaxed fragments. But if the cracks in adjacent rings line up like "cherries in a one-armed bandit," then longer strips will be formed when the cylinder tears apart, and the strip lengths will be equal to H times the number of lined-up rings.

To quantify our slot machine model, we must define what lined up means, and assign probabilities to the various degrees of alignment, as was done in the crack ladder case. As shown in Figure 2-20, if two half-penny bands approach each other in the same Mode 1 orientation, they can coalesce if they are in the same plan, which in practice means that the PZs (regions of strain concentration at the band tips) overlap. This criterion for coalescence is the same as for the tensile cracks, and is illustrated in Figure 2-21. Thus, the probability that two adjacent rings are aligned might appear to be

$$p(2H) = PZ/S \qquad (2.28)$$

where p(2H) is also the fraction of cracks with strip lengths greater than or equal to 2H, because when each ring is pulled apart, the shear bands will completely penetrate the ring to separate it. However, we must recall that only half the coalescing Mode 1 bands will be in the same 45 degree orientation, so in fact

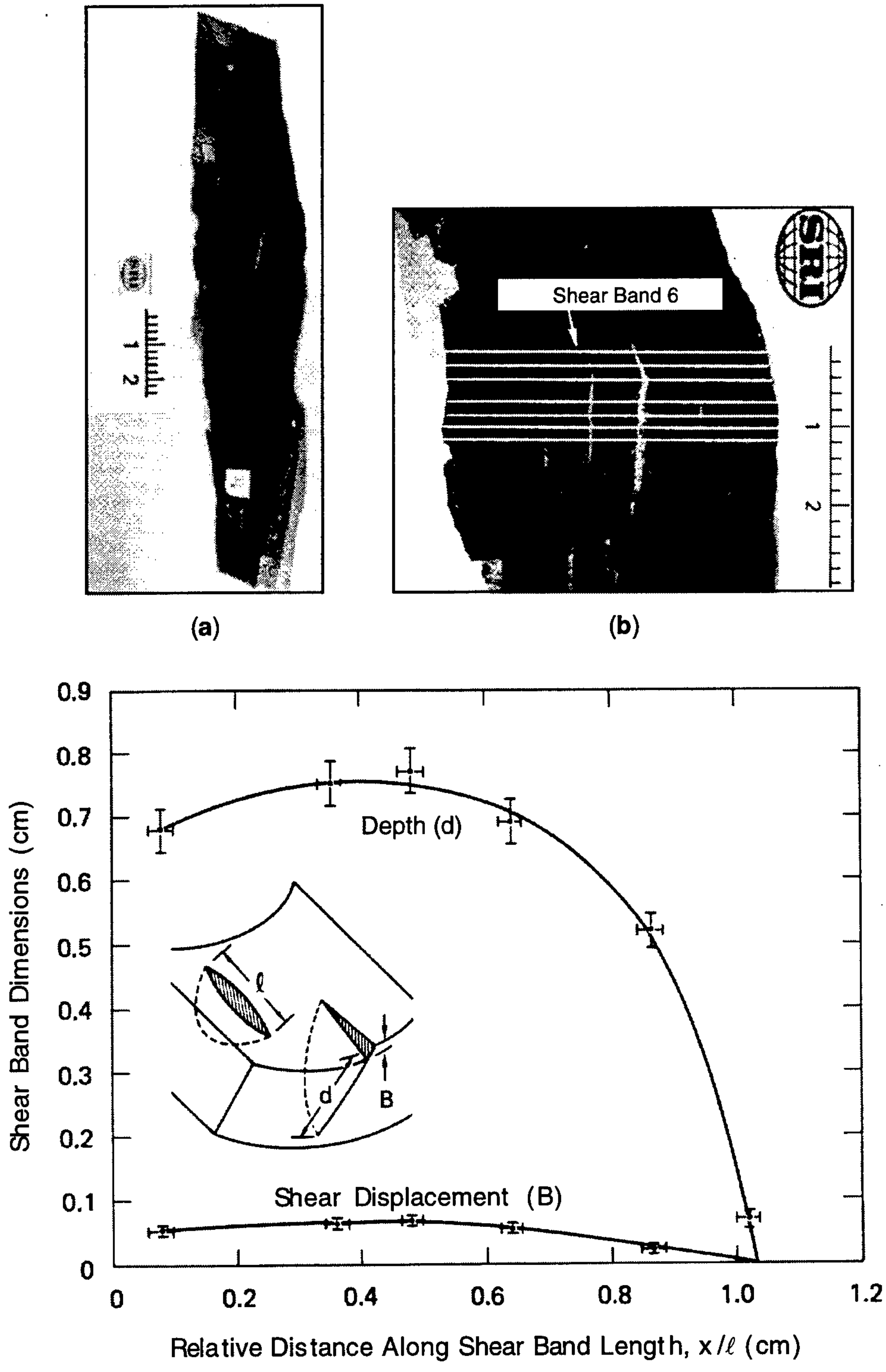

(a) (b)

(c)

Figure 2-17. Fragments (a) and (b) used in sher band profile study, and measured profile (c) of Shear Band 6.

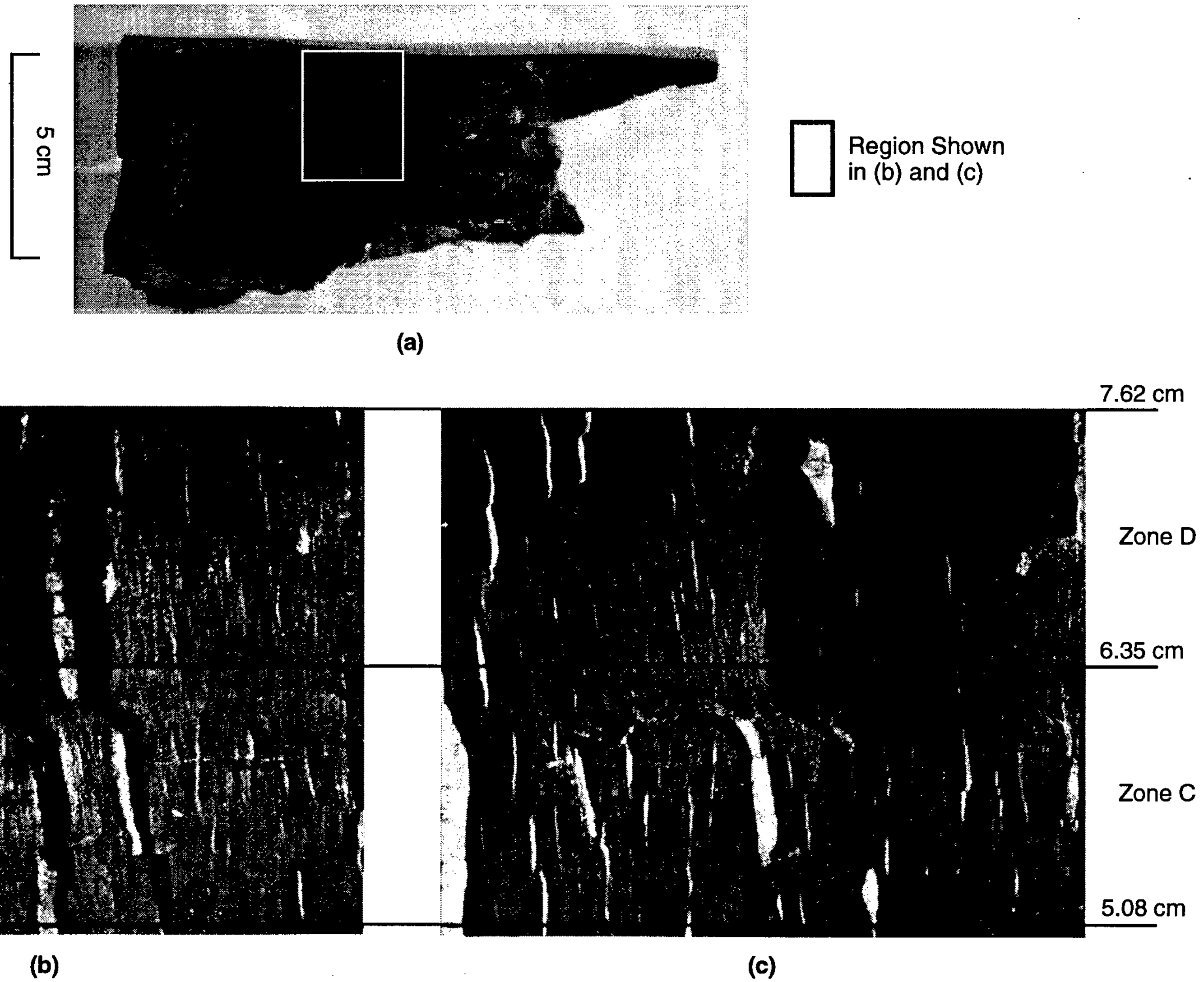

Figure 2-18. Recovered fragment (a) and photomicrographs (b and c) of two zones for use in quantitative shear band study. Note shading differences between (b) and (c). Distances are from end of cylinder.

(a)
Orientation Mode 1

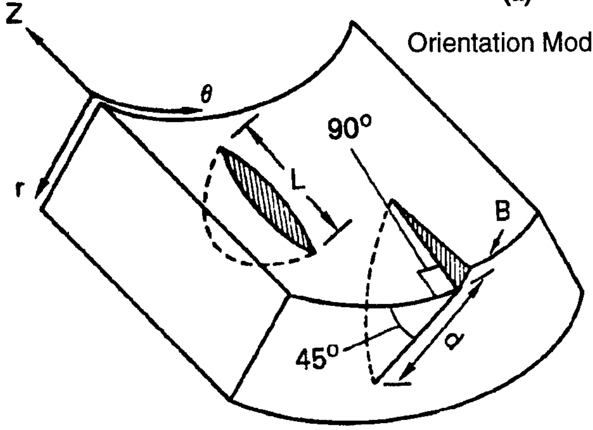

(b)
Orientation Mode 2

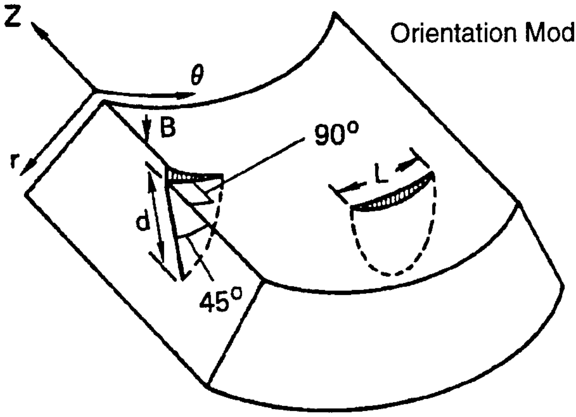

(c)
Orientation Mode 3

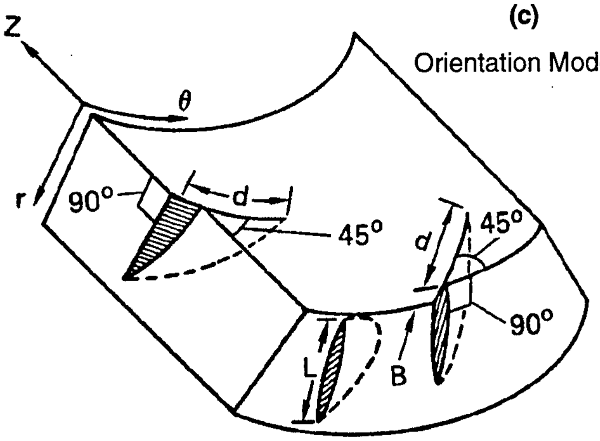

L – Length in Direction Perpendicular to Slip Motion

d – Depth Along 45° Slip Plane

B – Shear Displacement Along Slip Plane

Z – Axial Direction

r – Radial Direction

θ – Circumferential Direction

Figure 2-19. Geometry and nomenclature for shear bands in fragmenting cylinder experiments.

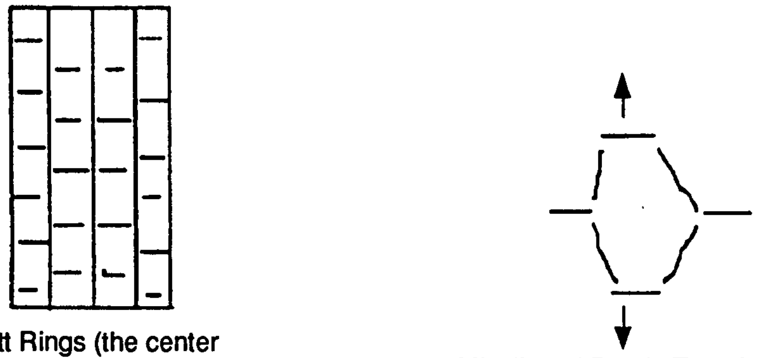

Mott Rings (the center rings are aligned)

Misaligned Bands Tear Apart to Form Equiaxed Fragments

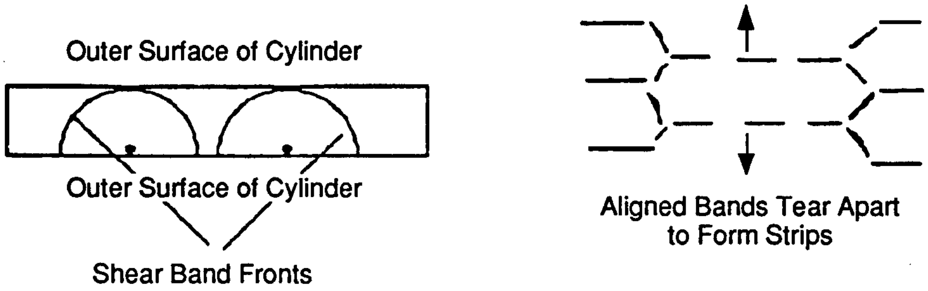

Aligned Bands Tear Apart to Form Strips

Figure 2-20. Basis of slot machine model.

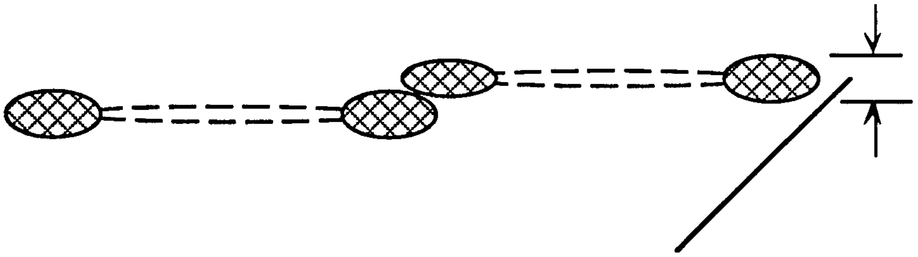

Shear Band Process Zone Size, Pz

Shear Bands Coalesce If Their Process Zones Overlap

Figure 2-21. Shear band coalescence.

$$p(2H) = PZ/2S \tag{2.29}$$

The probability that three adjacent rings line up is $(PZ/2S)^2$, and so on, so

$$p(nH) = (PZ/2S)^{n-1}$$

Thus, the fraction of strips of length greater than or equal to nH is

$$Ng(n)/N = (PZ/2S)^{n-1} \tag{2.30}$$

where Ng(n) is the number of fragments with aspect ratios greater than or equal to n, N is the total number of fragments, and the aspect ratio n is the strip length divided by the wall thickness H.

As discussed by Shockey et al. (1985]) dimensional analysis and computational simulations show that (in the absence of rate-dependence of Y) PZ is proportional to the shear band length (equal to H at coalescence), with a proportionality factor on the order of 1/4 to 1/2 (see Figure 2-21). Thus,

$$PZ/2 = \beta H \tag{2.31}$$

where $\beta \approx 1/8 - 1/4$. On the other hand, study of the fragments in Figure 2-12 shows that intersecting shear bands of opposite 45 degree orientations sometimes combine to make strips, in contradiction to the assumption behind Eq. (2.29). In such cases, β would be doubled. It appears best to allow β to be an adjustable parameter in the range of 1/8 to 1/2.

Combining (2.30) and (2.31) yields

$$Ng(n)/N = (\beta H/S)^{n-1} \tag{2.32}$$

2.3.4 Fragment Velocity Distribution.

For a zero-order approximation, we assume that the incipient fragments are accelerated until the cracks allow gas blow-by, at which time the gas pressure on the inner surface of the fragments drops significantly, and acceleration essentially ceases. This assumption must be checked by computer simulations but appears plausible because stagnation pressures would appear to be much less than the several GPa levels initially exerted by the detonation products.

The time required for this pressure drop is on the order of the time required for the gas to flow around the fragment. The initial gas velocity is equal to the fragment velocity, u, so the fragment unloading time = As/u, where A is an adjustable parameter on the order of unity (when the gas originally behind the fragment has expanded a distance s, the gas volume has increased by a factor of 4, and, for a γ of 1.2, the equilibrium pressure has dropped by a factor of 5).

Because the unloading time depends on fragment size, the smaller fragments will be unloaded while the larger fragments are still being accelerated. The velocity spread between the larger, faster fragments and the smaller, slower fragments is thus given by

$$\Delta u = (\partial u/\partial r)\Delta r = (\partial \varepsilon/\partial t)u\Delta t = A(\partial \varepsilon/\partial t)(s_{max} - s_{min}) \qquad (2.33)$$

For a typical case where the strain rate is about 1.5 x 10^4/s, and for fragment sizes ranging from 1 cm to 1 mm, Eq. (2.33) gives a fragment velocity range of 1.5 x 10^4 cm/s to 0.15 x 10^4 cm/s (for A = 1). Equation (2.33) needs to be compared with experimental data.

2.3.5 Conclusions for Explosive-Induced Fragmentation.

The simple dimensional analysis presented above suggests that the fragment shape distribution depends critically on the shear band process zone width, PZ = 2βH. Because PZ is not an easily obtained material property, we must consider β to be an adjustable parameter. However, if the values of β required to fit data become significantly different than about 1/4 (e.g., >1), the underlying assumptions of the theory will become suspect. Similarly, if the data show that the largest fragments do not, in fact, outrun the smaller fragments, the assumptions leading to Eq. (2.33) are not valid. Validation of both models must await comparisons with experimental data.

SECTION 3

SUMMARY OF SUGGESTED FRAGMENTATION ALGORITHMS

3.1 STRESS WAVE-INDUCED FRAGMENTATION.

The input to the algorithm is the material microscopic flaw size distribution, the material fracture toughness, the material density, the material sound speed, and the average strain rate during the impact event. The average fragment size is then obtained from Eq. (2.9) or Figure 2-1, and the fragment size distribution is obtained from Eq. (2.10). The fragment shape and area distributions are obtained from Eqs. (2.16), (2.17), and (2.21).

3.2 PLASTIC STRUCTURAL DEFORMATION-INDUCED FRAGMENTATION.

The input to the algorithm is the same as above except that we no longer use the microscopic flaw size distribution, but instead obtain the average fragment size and size distribution from Eqs. (2.6) and (2.10), with s_{min} obtained from the spacing between plastic strain concentrations. As for stress wave cracks, the fragment shape and area distributions are obtained from Eqs. (2.16), (2.17), and (2.21).

3.3 EXPLOSIVE-INDUCED FRAGMENTATION.

The input target material properties are the density, specific heat, thermal diffusivity, the thermal softening curve, and the shear band tip factor β. The fragment size distributions are obtained from Eqs. (2.23) through (2.26). The fragment shape distribution is obtained from Eq. (2.32). The fragment velocity distribution is obtained from Eq. (2.33).

3.4 DISCUSSION.

The new fragmentation algorithms presented above differ from those currently in the FAST/FACT code mainly in that they depend more on material properties and on the average strain rate in the target material rather than on specific energy coupled to the target material. Because the average strain rate in the target material is probably easier to guess in many cases than the coupled energy, it may in fact be easier to apply the new algorithms than the old ones. For example, a very rough estimate of the strain rate when a massive impactor hits a smaller target component is the impactor speed divided by the characteristic target dimension.

SECTION 4

COMPARISON WITH CURRENT DATA BASE

We have not yet correlated the above algorithms with data bases such as those in the report by McKnight et al. (1994). The obvious next step is to correlate the above strain rate-dependent algorithms with the specific energy algorithms in the FAST/FACT approach, using the codes of Eqs. (2.1) and (2.2).

SECTION 5

RECOMMENDED FUTURE DIRECTIONS

As a continuation of our work, we recommend a systematic effort to correlate the above algorithms with the current data base, and to extrapolate predictions outside the data base. This effort would consist of three steps:

(1) Use the approach of Eqs. (2.1) and (2.2) to convert the FAST/FACT correlations to those based on our new algorithms.

(2) Use the new algorithms to correlate with additional data not used in the report by McKnight et al. (1994).

(3) Use the new algorithms to address fragmentation and scaling issues outside the current data base.

SECTION 6

REFERENCES

Aharony, A., and A. Levi, "Percolation Model Calculations of Fragment Properties," *Annals of the Israel Physical Society* **8,** 1986. (UNCLASSIFIED0

Brosee, M. O., and M. P. Bermudez, "Lethality and Target Hardening Code Bibliography," prepared by Kaman Sciences Corporation, 2560 Huntington Ave., Alexandria, VA 22310, for the Defense Nuclear Agency/SPSP, April 1994. (UNCLASSIFIED)

Curran, D. R., and L. Seaman, "Simplified Computational Models of Fracture and Fragmentation," Contributed chapter in *Dynamic Fracture and Fragmentation,* Springer-Verlag, in preparation, 1993. (UNCLASSIFIED)

Curran, D.R., D. A. Shockey, L. Seaman, and M. Austin, in *Proceedings of the Symposium on Planetary Cratering Mechanics - Impact and Explosion Cratering*, D. J. Roddy, R. O. Pepin, and R. B. Merrill, eds., 1057-1088, Pergamon Press, 1977. (UNCLASSIFIED)

Curran, D. R., L. Seaman, and D. A. Shockey, *Physics Reports* **147**(5 and 6), 1987. (UNCLASSIFIED)

Deve, H., S. Harren, C. McCullough, and R. J. Asaro, *Acta Metall.* **36**(2), 341-365, 1988. (UNCLASSIFIED)

Erlich, D. C., D. R. Curran, and L. Seaman, "Further Development of a Shear Band Model," Final Report to the Army Materials and Mechanics Research Center, Contract No. DAAG46-77C-0043, Report No. AMMRC TR 80-3, March 1980. (UNCLASSIFIED)

Grady, D. E., and M. E. Kipp, *J. Appl. Phys.* **58**, 1210, 1985. (UNCLASSIFIED)

Grady, D. E., and M. E. Kipp, *J. Mech. Phys. Solids* **35**(1), 95-118, 1987. (UNCLASSIFIED)

Harren, S. V., and R. J. Asaro, *J. Mech. Phys. Solids* **37**(2), 191-232, 1989. (UNCLASSIFIED)

McKnight, D., R. Maher, and L. Nagl, "Fragmentation Algorithms for Satellite Targets (FAST) Empirical Breakup Model," Version 3.0, prepared by Kaman Sciences Corporation for Defense Nuclear Agency/SPSP, January 1994. (UNCLASSIFIED)

Meyers, M. A., K. S. Veccio, and U. Andrada, *Proceedings of the Symposium on Shear Bands and Viscoplastic Theories,* USCD, La Jolla, CA, September 14-19, 1992, to be published as a separate volume of the Mechanics of Materials, 1993. (UNCLASSIFIED)

Mott, N. F., *Proc. Roy. Soc. London A* **189**, 300-308, 1947. (UNCLASSIFIED)

Shockey, D. A., C. F. Peterson, D. R. Curran, and J. T. Rosenberg, "Failure of Rock under High Rate Tensile Loads - New Horizons in Rock Mechanics," *Proceedings of the 14th Symposium on Rock Mechanics*, Pennsylvania State University, University Park, PA, 709-738, 1972. (UNCLASSIFIED)

Shockey, D. A., D. R. Curran, and L. Seaman, "Development of Improved Dynamic Failure Models," Final Report to U.S. Army Research Office, Contract No. DAAG-29-81-K-0123, 1985. (UNCLASSIFIED)

DISTRIBUTION LIST

DSWA-TR-96-20

DEPARTMENT OF DEFENSE

BALLISTIC MISSILE DEFENSE ORGANIZATION/AQT
ATTN: CDR HAGGERTY
ATTN: DAN WHITENER
ATTN: DOUG SCHAEFER

DEFENSE INTELLIGENCE AGENCY
ATTN: G WEBER

DEFENSE SPECIAL WEAPONS AGENCY
2 CY ATTN: ISST
3 CY ATTN: CDR KENNETH HUNTER

DEFENSE TECHNICAL INFORMATION CENTER
ATTN: DTIC/OCP

FIELD COMMAND DEFENSE SPECIAL WEAPONS AGENCY
ATTN: DR BALADI

DEPARTMENT OF THE ARMY

U S ARMY SPACE STRATEGIC DEFENSE CMD
ATTN: LIBRARY

USASSDC
3 CY ATTN: R BECKER

DEPARTMENT OF THE NAVY

NAVAL SURFACE WARFARE CENTER
ATTN: CHARLES R ELLINGTON

DEPARTMENT OF THE AIR FORCE

USAF
ATTN: RON HUNT

DEPARTMENT OF ENERGY

LAWRENCE LIVERMORE NATIONAL LAB
ATTN: G POMYKAL

LOS ALAMOS NATIONAL LABORATORY
ATTN: J V REPPA

SANDIA NATIONAL LABORATORIES
ATTN: ERIC REECE

DEPARTMENT OF DEFENSE CONTRACTORS

ARES CORP
ATTN: CHUCK MARTIN

BATTELLE MEMORIAL INSTITUTE
ATTN: C ALEXANDER

KAMAN SCIENCES CORP
ATTN: VERN SMITH

KAMAN SCIENCES CORP
ATTN: DENNIS JONES

KAMAN SCIENCES CORPORATION
ATTN: DASIAC

LOGICON R & D ASSOCIATES
ATTN: D GAKENHEIMER

LOGICON R & D ASSOCIATES
ATTN: E TOTON

MAXWELL LABORATORIES INC
ATTN: DR. G GURTMAN

SRI INTERNATIONAL
2 CY ATTN: D CURRAN
2 CY ATTN: J COLTON

W J SCHAFER ASSOCIATES INC
ATTN: J CHERNAULT